JGR Oceans

RESEARCH ARTICLE
10.1029/2018JC014679

The Role of Eddies and Topography in the Export of Shelf Waters From the West Antarctic Peninsula Shelf

J. Alexander Brearley[1], Carlos Moffat[2], Hugh J. Venables[1], Michael P. Meredith[1], and Michael S. Dinniman[3]

[1]British Antarctic Survey, Cambridge, UK, [2]School of Marine Science and Policy, University of Delaware, Newark, DE, USA, [3]Center for Coastal Physical Oceanography, Old Dominion University, Norfolk, VA, USA

Key Points:
- Topographic bank at the mouth of Marguerite Trough preferentially retains cool, modified shelf waters
- Much of this cool shelf water is found in small cyclonic eddies generated by barotropic and baroclinic instabilities of the shelf break current
- These eddies play a key role in the heat budget of the shelf

Correspondence to:
J. A. Brearley,
jambre@bas.ac.uk

Citation:
Brearley, J. A., Moffat, C., Venables, H. J., Meredith, M. P., & Dinniman, M. S. (2019). The Role of Eddies and Topography in the Export of Shelf Waters From the West Antarctic Peninsula Shelf. *Journal of Geophysical Research: Oceans*, *124*. https://doi.org/10.1029/2018JC014679

Received 18 OCT 2018
Accepted 10 OCT 2019
Accepted article online 23 OCT 2019

Abstract Oceanic heat strongly influences the glaciers and ice shelves along West Antarctica. Prior studies show that the subsurface onshore heat flux from the Southern Ocean on the shelf occurs through deep, glacially carved channels. The mechanisms enabling the export of colder shelf waters to the open ocean, however, have not been determined. Here, we use ocean glider measurements collected near the mouth of Marguerite Trough (MT), west Antarctic Peninsula, to reveal shelf-modified cold waters on the slope over a deep (2,700 m) offshore topographic bank. The shelf hydrographic sections show subsurface cold features (θ <=1.5 °C), and associated potential vorticity fields suggest a significant instability-driven eddy field. Output from a high-resolution numerical model reveals offshore export modulated by small (6 km), cold-cored, cyclonic eddies preferentially generated along the slope and at the mouth of MT. While baroclinic and barotropic instabilities appear active in the surrounding open ocean, the former is suppressed along the steep shelf slopes, while the latter appears enhanced. Altimetry and model output reveal the mean slope flow splitting to form an offshore branch over the bank, which eventually forms a large (116 km wide) persistent lee eddy, and an onshore branch in MT. The offshore flow forms a pathway for the small cold-cored eddies to move offshore, where they contribute significantly to cooling over the bank, including the large lee eddy. These results suggest eddy fluxes, and topographically modulated flows are key mechanisms for shelf water export along this shelf, just as they are for the shoreward warm water transport.

Plain Language Summary The glaciers and ice shelves of the West Antarctic Peninsula have been rapidly retreating in the past 50 years, believed to be driven by increasing fluxes of heat from the ocean. While knowledge of the mechanisms that drive this heat from the open ocean onto the continental shelves has improved, our understanding of the counterbalancing flows of shelf waters remains limited. In this study, temperature, salinity, and velocity observations from an underwater autonomous vehicle, alongside numerical model output, are used to elucidate the pathway and mechanisms by which shelf waters are moved into the ocean interior. Small spinning vortices—known as eddies—containing shelf water are periodically generated from dynamical instabilities that derive from the horizontal shear of the flow. These small eddies then move offshore to cool a region of elevated topography near the mouth of Marguerite Trough, a deep glacially carved canyon. Here, cold water accumulates in a larger persistent eddy; satellite observations suggest that this water may ultimately be discharged into the Southern Ocean interior. Given that the topographic conditions of the field site are not unique, eddies and topographic flows are likely key mechanisms that balance the onshore flux of ocean heat in the West Antarctic.

1. Introduction

The West Antarctic Peninsula (WAP) in the Bellingshausen Sea is one of the most climatically variable environments on Earth. Since the middle of the twentieth century, significant atmospheric, oceanographic, and cryospheric changes have occurred. First, atmospheric temperatures have shown the largest average atmospheric warming in the Southern Hemisphere during the twentieth century, with warming of ~0.5 °C per decade between the 1950s and 1990s, a trend particularly strong during winter (King et al., 2013; Vaughan et al., 2003). However, since 2000, there has been an absence of statistically significant atmospheric warming (though the overall positive trend from 1950 to 2014 is still statistically significant; Turner et al., 2005, 2016). Second, the extent and duration of sea ice cover in the Bellingshausen Sea decreased rapidly since the start of the satellite era (Stammerjohn et al., 2008), though since 2000 the

northern part of the WAP has seen sea ice increases (Turner et al., 2016). The overall trend is divergent from other parts of Antarctica such as the Ross Sea, where long-term increases in sea ice extent have been observed (Comiso et al., 2016). The glaciers of the West Antarctic have retreated rapidly (Cook et al., 2005, 2016), and the rate at which ice sheets have been losing mass has increased (Rignot et al., 2014; Rignot et al., 2019). Summertime temperatures in the upper water column increased by more than 1 °C between the 1950s and 1990s (Meredith & King, 2005) with deep warming on the shelf being observed by Schmidtko et al. (2014). Significant freshening is apparent close to the coast, where glacial meltwater is a significant input, but further offshore upper layer salinification has been observed (Bers et al., 2013; Schloss et al., 2012).

Unraveling cause and effect of many of these changes remains challenging. However, a consensus has emerged that many of the glacial and ice sheet losses are driven by greater delivery of heat from the Upper Circumpolar Deep Water (UCDW), a water mass that typically resides below 200 m on the continental shelf (Jacobs et al., 2011). UCDW, generally characterized as having potential temperatures exceeding 1.7 °C and salinities greater than 34.54, originates as strongly modified Pacific and Indian Ocean waters (Callahan, 1972). However, around West Antarctica it forms a key constituent water mass of the Antarctic Circumpolar Current (ACC) that resides offshore of the continental shelf. To access the shelves, and ultimately the ocean cavities beneath the floating ice shelves, this water mass must cross the Southern ACC front (Orsi et al., 1995) that here closely follows the southern boundary of the ACC and then be advected onshore toward the Peninsula coast (indeed, the southern boundary is often defined as the southern limit of the UCDW). As it does so, it is modified by both isopycnal and diapycnal mixing, including with the overlying Winter Water (WW). This latter water mass, formed by a combination of wintertime sensible heat loss, deep vertical mixing and sea ice growth, persists throughout the year but is capped during summertime by a thin layer of freshwater caused by seasonal melt and warmed by atmosphere-to-ocean heat fluxes.

Extensive literature now exists detailing possible mechanisms by which UCDW transits onto the shelves. Prezelin et al. (2000) argued that UCDW is delivered primarily though wind induced or topographically induced upwelling, with Martinson et al. (2008) arguing that heat content on the shelf is higher where isopycnals are elevated; however, this may also be a signature of eddy variability. Alternatively, Dinniman and Klinck (2004) and Dinniman et al. (2011) argue that flow inertia is key mechanism delivering intrusions of UCDW to the shelf. The shelf itself is punctuated by a number of deep glacially carved troughs, the largest of which is Marguerite Trough (Figure 1a), which reaches up to 1,600 m deep and 35 km wide. A strong northeastward flowing current exists along the shelf break, the southern boundary of the ACC (Dinniman & Klinck, 2004). When this topographically controlled flow is sufficiently strong, it appears able to cross the strong seaward bend in the shelf geometry close to the mouth of Marguerite Trough (MT), allowing the UCDW to flood into the bottom of the trough. This conclusion is supported by high-resolution modeling (Graham et al., 2016), who estimated a heat flux of $28.4 \pm 25.2 \times 10^4$ W/m^2 into MT using a simulation with a ~1.5-km horizontal grid spacing.

However, in recent years, small mesoscale eddies of UCDW have emerged as the most prominent mechanism by which UCDW heat is delivered onto the shelves. Moffat et al. (2009) argued that previous studies based on coarsely spaced data such as from ship-based hydrographic surveys have introduced a sampling bias, allowing the signature of multiple small eddies to be misinterpreted as broader-scale intrusions. The currents typically associated with these eddies are relatively weak (1–2 cm/s). A follow-up study using mooring-based observations (Martinson & McKee, 2012) roughly halfway up MT documented an average of around 40 eddies per year from 2007 to 2010, with an average diameter of 8–10 km. More recently, a broad-scale census of these features has been carried out across the WAP shelf by Couto et al. (2017). Combining several years of underwater glider surveys conducted from the Palmer Long-Term Ecological Research program, they conclude that 60% of the glider profiles containing UCDW were part of a coherent eddy. MT was identified as a highly important pathway for these eddies, with 20–53% of the total lateral onshore heat flux reaching the shelf up this canyon.

While a detailed description of the location and scale of eddies drawing UCDW ashore has now been achieved, significant uncertainty remains over the location and mechanisms by which such eddies are generated. Proposed candidates for eddy generation include both baroclinic and barotropic instability of the shelf break jet (McKee et al., 2019), as well as topographic instabilities generated by the interaction of the jet with the continental shelf. Furthermore, recent advances in high-resolution modeling (St-Laurent

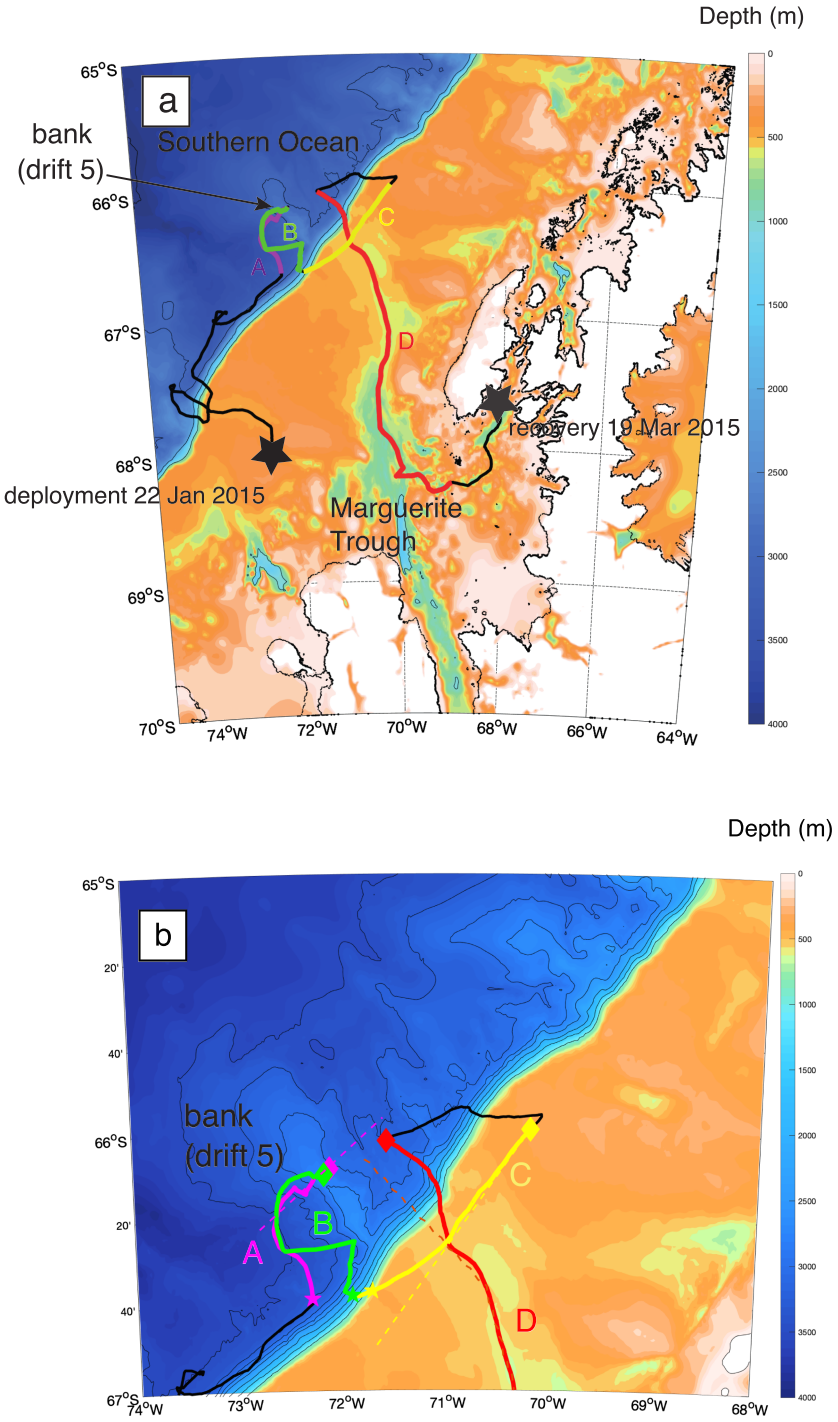

Figure 1. (a) Map of study region. This shows the glider track with deployment and recovery dates and positions, along with the four observational sections referred to in subsequent figures. Bathymetry from the International Bathymetric Chart of the Southern Ocean is plotted, with 1,000-, 2,000-, and 3,000-m contours highlighted. (b) Zoom-in of the mouth of Marguerite Trough. The beginning of each section (0-km horizontal distance) is shown with a star, and the end of each section is shown with a diamond marker. Drift 5—the bank—is also marked. Solid contours are at 1,000, 1,500, 2,000, 2,500, 2,750, 3,000, 3,250, and 3,500 m. The model sections approximating the observational lines A, C, and D are also marked with dashed lines.

et al., 2013) have suggested that the interaction of a broad jet with the mouth of a trough (such as MT) may set up a dominantly cyclonic circulation, bringing warm water onshore toward the northeastern side of the trough and exporting cold and fresh water toward the southwest. Furthermore, Rossby waves interacting with the shelf break can also produce eddy-like features that then propagate inshore on the eastern side of the trough (Zhang et al., 2011). Residual mean theory (Plumb & Ferrari, 2005) has also been invoked as a possible mathematical formulation for understanding the flux of deep eddies onshore (Stewart & Thompson, 2015; Thompson et al., 2014), though the theory is best developed for regions where dense bottom waters are moved offshore in the deepest layers, a process absent on the western side of the Antarctic Peninsula.

Conservation of mass dictates that the warm water drawn onshore either by eddies or intrusions must be compensated by an offshore flow of shelf water. Comparatively, little attention has been given to these compensating offshore flows, yet the exchange of deep waters between the shelves and the open Southern Ocean is key to both heat and nutrient budgets of the WAP shelves. The limited observations that do exist (Moffat et al., 2009; Savidge & Amft, 2009) suggest that a significant offshore flow is found on the southern side of the trough, with onshore flows dominantly at the northern side of the trough. The pattern of these flows is linked closely to the shelf break front and associated surface-intensified jet, which advects water northeastward along the shelf break. Modeling and limited observational evidence also points to a possible deep, southwestward flowing countercurrent under this shelf break current (Graham et al., 2016; Hillenbrand et al., 2008).

It has long been established that many shelf break fronts exhibit unstable behavior, with large meanders forming and individual eddies being observed to pinch off and form separate rotating vortices. These features were noted in early submarine observations (Wadhams et al., 1979). Such eddies have been shown to be key vectors for the transport of heat and nutrients into the ocean interior in many locations. Instability mechanisms that drive the detachment of eddies from such boundary currents have been uncovered in a series of idealized model and tank experiments. Early work focused on instabilities that could develop over a flat ocean bottom with baroclinic instability (Charney, 1947) being identified as the key mechanism driving the detachment of eddies from a buoyancy-driven coastal current (Griffiths & Linden, 1981). However, many such currents, including the Antarctic Slope Front, are instead located over continental slopes. The baroclinic instability of a front over steep topography was first investigated by Flagg and Beardsley (1978). Unstable modes were present over steep topography, but the *e*-folding times of these instabilities increased from 2 to 5 days over a flat bottom to 50 days over rough topography. More recently, several investigators have studied the effect of topography sloping in different directions on the stability of the boundary current. Reszka and Swaters (1999) found that topography sloping in the same direction as the front tended to stabilize the water column, while a front sloping in the opposite sense of the front tended to enhance the baroclinic instability. More recently, Cenedese and Linden (2002), using a tank experiment, found that the presence of topography within a boundary current system introduced a second mode of instability, with the relevant controlling parameter being the difference between the width of the boundary current at the onset of the instability and the continental shelf width. Stewart and Thompson (2013), in an idealized channel setup representative of the Southern Ocean, found that baroclinic instability tended to be suppressed over the continental slope.

In this paper, we use high-resolution underwater glider measurements taken during February and March 2015 to investigate in detail the flow structure around the mouth of MT and to understand how the interaction of the boundary current with the mouth of MT affects the offshore export of deep shelf waters into the open Southern Ocean. Satellite altimeter data covering a 24-year period (1993–2016) and output from a 1.5-km horizontal resolution Regional Ocean Modeling System (ROMS) model of the area are also used to extend the spatial and temporal scale of the glider data. The paper is arranged as follows. The data acquisition, quality control, calculations, and model description are outlined in section 2. Section 3 describes the water mass structure and spatial fields of velocity and potential vorticity (PV) close to the mouth of MT from the glider and altimetry observations, diagnoses the likely instability mechanisms at play using the model output, and elucidates the properties of small, cyclonic eddies of cool shelf waters. The discussion in section 4 postulates the likely fate of this cool shelf water and assesses the relevance of these processes to the WAP shelf more widely. Conclusions and implications for the circulation and heat fluxes of the West Antarctic are outlined in section 5.

2. Data and Model Output

2.1. Bathymetry

Data from the International Bathymetric Chart of the Southern Ocean were used to investigate the topographic features around the mouth of MT (Arndt et al., 2013). This is a complex topographic region, with a deep glacially carved canyon punctuating the continental shelf. At its mouth, the trough is around 450 m deep, but it deepens significantly inshore, reaching almost 1,600 m deep close to the edge of George IV ice shelf (Figure 1). The continental slope itself is remarkably straight on the upstream (southwestern) side of the trough, but a large sedimentary drift deposit known as Drift 5 (Hillenbrand & Ehrmann, 2005; Rebesco et al., 1996) is found immediately upstream, elevated around 1,100 m above the abyssal floor. This is seen clearly in the 3,000-m isobath, which diverts 70 km offshore before rejoining the main continental slope at the mouth of MT itself (Figure 1b). On the downstream side of the trough, several further offshore excursions of the 3,000-m isobath are observed, associated with further sedimentary deposits. These features give the deep topography significantly stronger curvature than the shallower isobaths, which tend to be relatively straight. Limited current meter observations from Drift 7, further to the southwest, suggest a very deep narrow, southwestward current (sitting beneath the CDW) that advects mainly Weddell Sea Deep Water (Giorgetti et al., 2003; Hillenbrand et al., 2008). However, this current appears to be largely confined beneath 3,000 m, with the near-surface currents being northeastward directed. As demonstrated later, this bathymetry strongly affects the overall PV structure. For the purposes of this paper we refer to Drift 5 as "the bank."

2.2. Glider Data

Temperature (T), salinity (S), pressure (P), and depth-averaged velocity data were collected from a Slocum 1,000-m pressure rated oceanographic glider incorporating a pumped conductivity-temperature-depth (CTD) instrument (serial number 409). The instrument was deployed from *R.V. Lawrence M. Gould* on 22 January 2015 and was recovered at Rothera, Adelaide Island, on 19 March 2015. Its 1,278-km-long track is shown in Figure 1. Following data download, a number of quality control steps were carried out. T and S were interpolated onto 1-dbar pressure levels and any T/S spikes removed. The despiking was performed through a combination of an automatic neighborhood despiking, followed by a manual inspection of the individual profiles. In the neighborhood despiking, T and S values were removed if they fell outside the range $q_1 - 2(q_3 - q_1) < T/S < q_3 + 2(q_3 - q_1)$, where q_1 and q_3 are the lower and upper quartiles of the chosen range, respectively. It was noticed during the deployment that 3 days of conductivity data around 2–5 February were affected by large offsets. We believe that this occurred from biological contamination of the conductivity cell, which biased the conductivity unrealistically low for the period. However, after flushing of the cell, the contamination was cleared from the cell and conductivity returned to values comparable with those observed prior to the contamination event. To test this, glider T and S were compared with high-quality CTD data collected at the start and end of the deployment, one from *R.V. Lawrence M. Gould* and one from small boat work conducted as part of the long-term Rothera Time Series (Venables & Meredith, 2014). The *Gould* time series is accurate to 0.001 °C in temperature and 0.002 in salinity, while RaTS is accurate to 0.002 °C in temperature and 0.005 in salinity. No systematic difference between glider and ship-based CTDs could be observed at the start of the series, but the profiles collected after the contamination incident had an offset in conductivity by −0.003 mS/m. These data were corrected accordingly. Finally, in order to test whether there was a significant issue with thermal lag, sequential upward and downward temperature profiles were compared using the SOCIB glider toolbox (Troupin et al., 2016). Owing to the pumped CTD, thermal lag effects were very small and corrections were minimal.

Calculating the full velocity fields requires an accurate estimate of the geostrophic reference velocity. The glider does not provide this directly, but careful processing of the depth-averaged velocities from the glider can yield an accurate reference velocity field. To achieve this, the glider compass was first calibrated using the procedure specified by the manufacturer to correct for heading-dependent offsets that were present in the data, and final x and y velocity vectors calculated to correct for surface drift (Merckelbach et al., 2010). Second, as a typical glider cycle is 6–8 hr, a period which can be affected significantly by, for example, inertial and semidiurnal tidal motions, the velocity data had to be processed before being used as a geostrophic reference. To do this, the glider velocities were detided using the regional Oregon State University TPXO tidal model for the Antarctic Peninsula (AntPen04.01) (http://polaris.esr.org/ptm_index.html). To remove

other high-frequency sources of velocity contamination, the detided velocities were then smoothed using a Laplacian spline interpolant over 15 km, with gridding at 5 km in the horizontal and 5 m in the vertical. Finally, the T and S fields were identically filtered before using the depth-averaged velocities to reference the T- and S-derived geostrophic shear.

To assess the sensitivity of the results to the detiding and smoothing procedures, we repeated the calculation of geostrophic velocities neglecting the detiding step and using a range of different filter length from 5 to 25 km. The barotropic tidal velocities are generally small (the mean magnitude of the tidal current speeds over the length of the deployment was 1.5 cm/s compared with 9.4 cm/s for the depth-averaged glider velocities). Smoothing at distances longer than 25 km led to unacceptable levels of smearing of important hydrographic features (e.g., the boundary current), but between 5 and 25 km the calculated velocity field was not strongly affected by the choice of smoothing length.

To assess the stability of the boundary current, the resultant buoyancy and velocity data from the gliders were then used to calculate the Ertel PV, following the methodology of Thompson et al. (2014). This decomposition breaks down the total PV (Q) into a stretching term dominated by the vertical stratification, a tilting term dominated by the lateral buoyancy gradient, and a lateral shear term dominated by the relative vorticity:

$$Q \approx f\frac{\partial b}{\partial z} + \frac{\partial u}{\partial z}\frac{\partial b}{\partial y} - \frac{\partial u}{\partial y}\frac{\partial b}{\partial z} \tag{1}$$

where f is the Coriolis parameter, y and z are the horizontal and vertical ordinates, and $b = -g(\rho - \rho_0)/\rho_0$, where b is the buoyancy, g is the gravitational acceleration, ρ is the neutral density, and ρ_0 is a reference density (1,025 kg/m^3). Note the simplification in this equation—the lateral gradients in both buoyancy and velocity are only calculated in the cross-track direction. This is a necessary approximation given the data; however, the effect of neglecting the other terms is shown to be small using the model in section 3.2.1, which uses both the along-stream and across-stream gradients.

In large-scale open ocean geostrophic flows, the stretching term dominates this vorticity structure. However, both the lateral shear and tilting terms have been shown to make significant contributions in boundary currents at open ocean margins, for example, in the Antarctic Slope Front (Thompson et al., 2014) and in the East Greenland Boundary Current (Brearley et al., 2012; Pickart et al., 2005).

2.3. High-Resolution Model Output

A high-resolution model run was used to complement the spatial and temporal scope of the glider observations. The circulation model for the WAP is based on the ROMS, a primitive equation, finite-volume ocean circulation model with a free surface, and a terrain-following vertical coordinate (Haidvogel et al., 2008; Shchepetkin & McWilliams, 2009). The configuration used here is the 1.5-km horizontal resolution model of Graham et al. (2016), which includes 24 variable-thickness vertical levels that are concentrated toward the top and bottom surfaces. Model bathymetry (bedrock depth and draft of any floating ice shelves) is from the Bedmap2 database (Fretwell et al., 2013). This model includes a dynamic sea ice model (Budgell, 2005), based on ice thermodynamics described by Mellor and Kantha (1989) and Häkkinen and Mellor (1992), an elastic-viscous-plastic rheology (Hunke, 2001; Hunke & Dukowicz, 1997), and a simple parameterization of frazil ice (Steele et al., 1989). The model also simulates mechanical (surface drag and depressed ocean free surface) and thermodynamic (heat and salt fluxes due to ice melt/freeze) interactions between the floating ice shelves in the model domain and the water cavity (Dinniman et al., 2011; Holland & Jenkins, 1999).

The results used here are from the same 1.5-km resolution run first discussed in Graham et al. (2016), except that the period of high-frequency (daily) model output has been extended from 1 to 2 years (2008–2009). Lateral open boundaries (details in Graham et al., 2016) are forced with observational-based temperature and salinity climatologies, ocean reanalysis velocities (Carton & Giese, 2008), and monthly (nonclimatological) satellite-based sea ice concentration. Tidal forcing is not included. Atmospheric forcing is from high-resolution (20 and 15 km) archived forecasts from the Antarctic Mesoscale Prediction System (Powers et al., 2012). The 1.5-km version of the model was shown to simulate well the locations of CDW intrusions

onto the continental shelf, and increasing the horizontal resolution to 1.5 km (from 4 km) was shown to be critical to accurately represent the heat content on the shelf.

2.4. Satellite Altimetry

To investigate further the dynamics of the boundary current and to suggest the likely fate of the shelf waters, 1/4° gridded sea surface height anomaly (SSHA), surface geostrophic velocities, and mean absolute dynamic topography (Rio et al., 2011) from AVISO were used. Due to some data dropouts in the SSHA fields, weekly data from January 1993 to December 2016 were averaged into monthly means and the resulting images (produced from the mean absolute dynamic topography and SSHA fields) assessed for the presence of meanders and mesoscale eddies close to the shelf break (in the box 64–66.5°S, 73–70°W). To achieve this, monthly mean SSH was contoured with 2 dyn. cm resolution, and these images inspected for the presence of closed contours in the vicinity of the bank. If an eddy was present in the monthly image, its diameter L and Rossby number $Ro = U/fL$ were calculated. This was achieved using a characteristic azimuthal velocity for each image and the best estimate of its radius using the distance between the two minima in velocity (at the edge and center of the eddy respectively). While this is necessarily an approximation and there is the potential for the mean to be slightly biased toward the longest-lived eddies (which are in the largest number of monthly images), the size of the tip eddies is relatively similar (and can only ever be known approximately owing to the horizontal resolution of the gridded altimetry).

3. Results

3.1. Hydrographic Structure and Circulation in MT and Shelf Slope From Glider Surveys

3.1.1. Hydrographic Properties

The potential temperature (θ) and salinity (S) sections, both off/onto the bank, and across and along MT, are shown in Figure 2. The location of each individual section is shown in Figure 1b, with timings included in Table 1, alongside the accompanying model sections. In addition, the θ/S plot for the same observational sections is shown in Figure 3. Clear differences in water mass characteristics are observed over the open ocean (3,900-m depth), compared with water over the bank (2700 m depth) (Figures 2a–2d). Specifically, the temperature of θ_{max} decreases significantly, from around 2.1 to 1.5 °C, while the θ_{min} of the WW layer cools from −1.4 to −1.7 °C, with the depth of θ_{min} increasing from ~60 to 120 m. In θ/S space (Figures 3a and 3b), there is a significant cooling along isopycnals onto the bank from the open ocean, both within the θ_{max} layer but also in much of the main thermocline. This illustrates that a water mass source for the deeper water over the bank is distinct from that found in the open Southern Ocean.

Examining the transect across MT (Figures 2e and 2g), a similar spatial differentiation in θ/S properties is observed. A clear gradient in the magnitude of θ_{max} can be seen transiting southwest to northeast across the mouth of the trough. While the portion in the open ocean (0–10 km along the baseline) has θ_{max} in the CDW of ~2.1 °C, the southernmost part of the trough section (10–40 km) generally has $\theta_{max} < 1.5$ °C. In contrast, θ_{max} on the northern bank of the trough (40–90 km) exceeds 1.7 °C in many of the profiles (black line in Figure 2e). In this part of the section there is evidence of three warm-cored features possessing $\theta_{max} >$ 1.7 °C, while only one is found toward the southern end of the trough, with $\theta_{max} < 1.6$ °C. The horizontal scale of these anomalies, between 5 and 15 km, is consistent with warm eddies observed previously in this region (e.g., Moffat et al. (2009); Martinson & McKee, 2012; Couto et al. (2017)). A similar gradient is seen when viewed in θ/S space: Profiles near the southern edge of the trough (but away from the open ocean) are generally colder along isopycnals than in the central (and to a lesser extent, the northern) portion of the trough (Figure 3c). Section D, aligned along MT, also exhibits a strong gradient in CDW properties (Figures 2f and 2h). It is apparent from Figure 2f that the shelf break is a strong barrier to the inflow of the warmest CDW, in line with the findings of several previous studies (e.g., Moffat et al., 2009; Graham et al., 2016). The typical θ_{max} within the trough is 1.3–1.4 °C, except within a few regions where $\theta_{max} >$ 1.5 °C is observed. Once again, it is likely that these features are CDW eddies. In addition, the depth of θ_{max} increases significantly onshore up the trough, from ~260 m near the shelf break to 420 m, 300 km inshore of the shelf edge. The θ/S diagram (Figure 3d) exhibits several notable features. The core of the UCDW around neutral density $\gamma_n = 27.95$ kg/m^3 cools with distance inshore, while the WW and overlying surface waters freshen significantly, such that the core of the WW is displaced from $\gamma_n = 27.6$ kg/m^3 near the

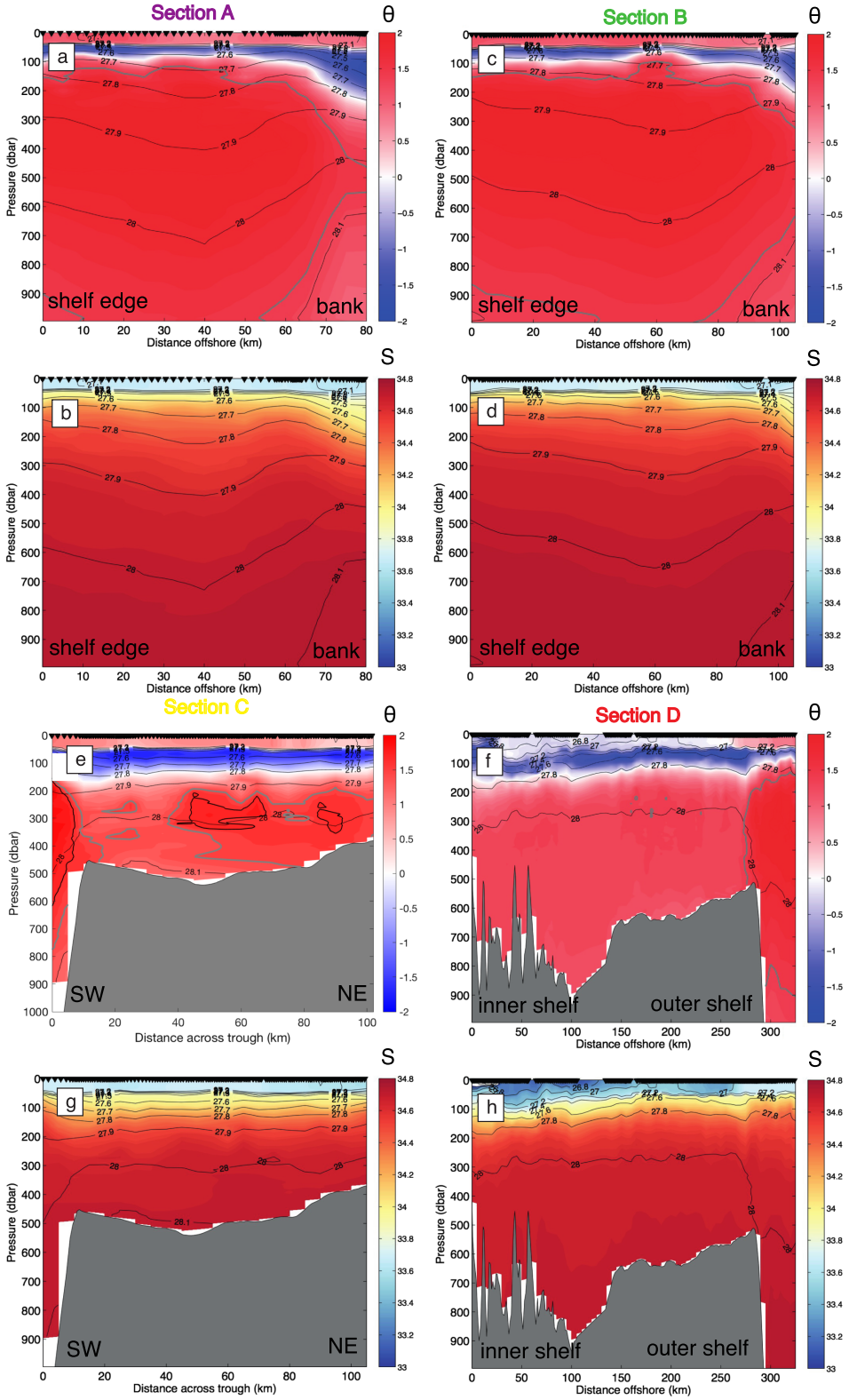

Figure 2. Potential temperature (θ) and salinity (S) sections for the four sections shown in Figure 1. The orientation of the x axes is positive onto the bank (Sections A and B), positive from southwest to northeast across the trough (Section C), and positive offshore (Section D)—see stars and diamonds in Figure 1a. The original glider profile locations are shown with inverted triangles. Contours of neutral density, in kilograms per cubic meter, are overlaid with black contours and the 1.5 °C isotherm is marked with a gray contour. An additional 1.7 °C isotherm is marked with a black contour in Figure 2e to illustrate the presence of Circumpolar Deep Water eddies more clearly.

Table 1
Start and Finish Times of Each Glider Section Shown in Figure 1 (UTC)

Section	Start date/time	End date/time
A	8 Feb 2015/2254	13 Feb 2015/1941
B	13 Feb 2015/2141	20 Feb 2015/2102
C	20 Feb 2015/2237	24 Feb 2015/1526
D	28 Feb 2015/0847	14 Mar 2015/2141

Note. UTC = coordinated universal time.

shelf break to $\gamma_n = 27.35$ kg/m^3 300 km up the trough. This change largely reflects the increased direct influence of glacial and sea ice melt in the near-surface layers as one approaches the coast.

The cooler and fresher deep waters found over the bank and on the southwestern side of the mouth of MT are consistent with CDW that has been modified by mixing and/or ventilation on the shelf and is hereafter referred to as modified CDW (mCDW). In contrast, the warmer water found toward the northeastern side of the trough has characteristics more consistent with unmixed CDW from the ACC further offshore, having undergone less intense shelf modification.

3.1.2. Circulation

Sections of glider-referenced geostrophic velocities (section 2.2) through the boundary current, over the bank, and within the mouth of the trough, are shown in Figure 4. A northeastward along-slope equivalent barotropic flow is found both on and just offshore of the shelf break, with typical velocities of around 10 cm/s in the near-surface layers (Figure 4a). As one moves onto the bank itself, the sign of the velocity field changes, with strong southwestward flows dominating, reaching a magnitude of up to 20 cm/s. Figure 4c demonstrates that the velocity vectors are closely following contours of f/H (where H is the water depth).

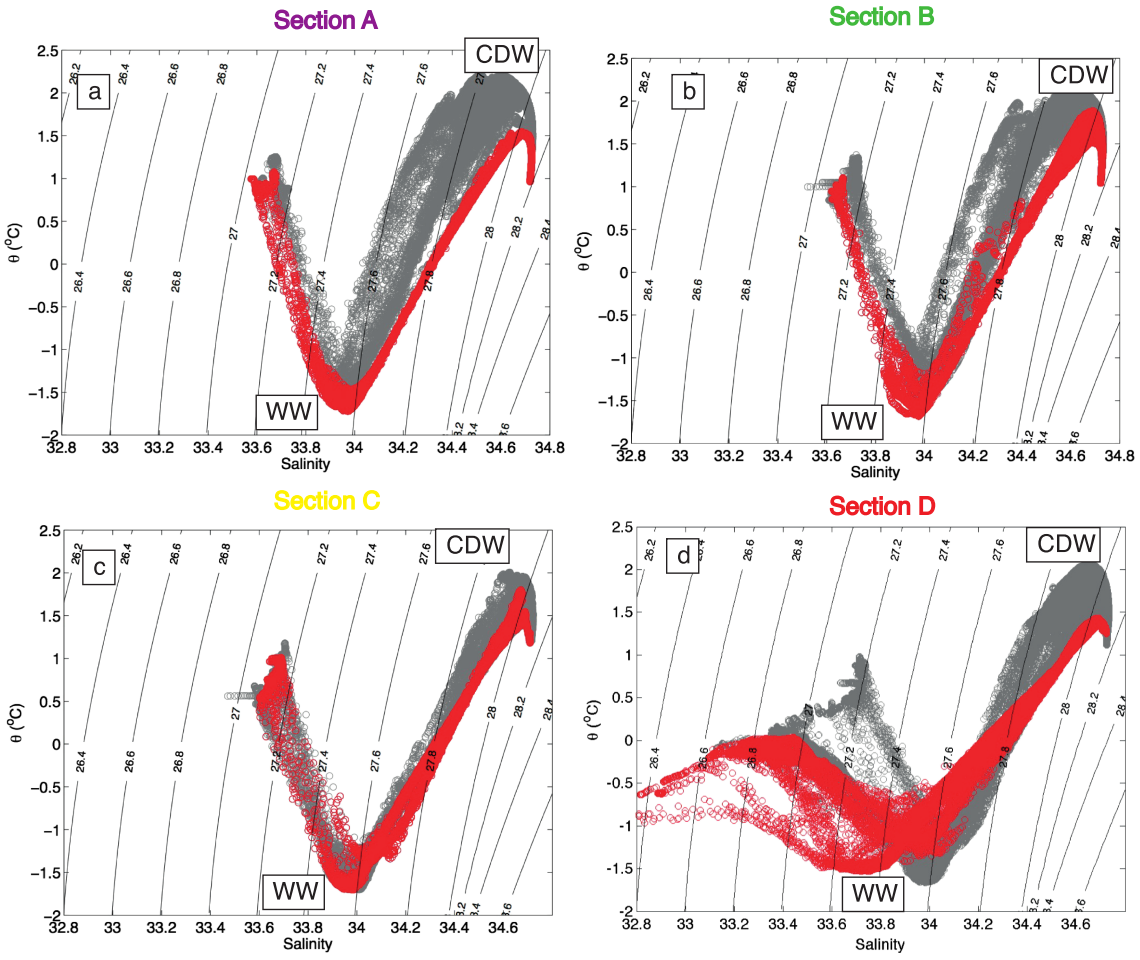

Figure 3. θ-S profiles for the four sections, with the main water masses marked. Contours of neutral density, in kilograms per cubic meter, are overlaid. For each section, red profiles denote (a) profiles at distances greater than 70 km along the baseline, over the bank; (b) profiles at distances greater than 95 km along the baseline, over the bank; (c) profiles at distances less than 30 km along the baseline, at the southern end of the trough; and (d) profiles at distances less than 100 km along the baseline, on the inner shelf. The cooler/fresher class of CDW found over the bank corresponds with water toward the southwestern edge of the trough and the inner shelf. CDW = Circumpolar Deep Water.

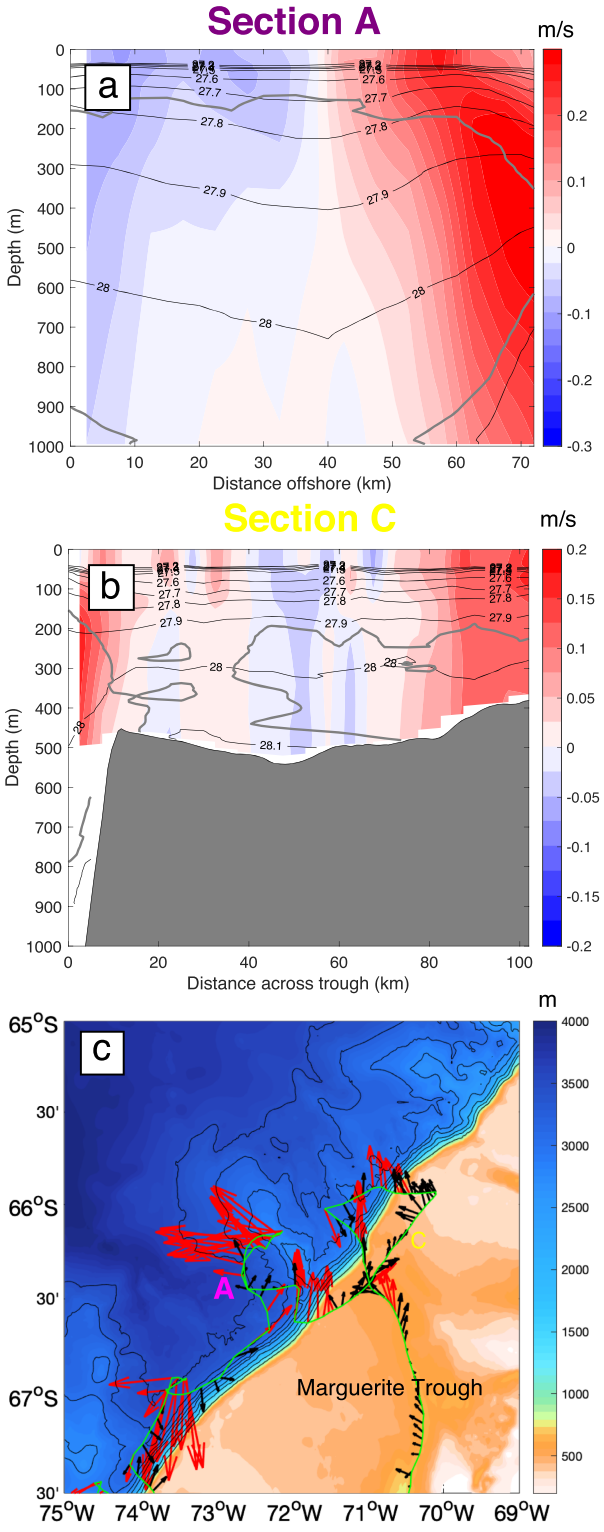

Figure 4. Glider-referenced geostrophic velocities for (a) Section A (positive is southwestward) and (b) Section C (positive is offshore), with neutral density contours shown. Regions where $\theta > 1.5$ °C is contoured in gray. (c) The glider track (in green) and glider depth-averaged velocities near the mouth of MT and over the bank (subsampled for clarity of the plot). Velocities of less than 10 cm/s are shown in black arrows, those exceeding 10 cm/s are shown in red. Contour intervals are as in Figure 1b.

The velocity section across the mouth of MT (Figure 4b) shows offshore flow (of up to 10 cm/s) toward the southern end of the section and close to the northern boundary, while the middle of the section has a much more variable velocity field. Flow is generally weakly onshore, but significant mesoscale variability over length scales of ~10 km exists, associated with the temperature maxima in the CDW layer described in section 3.1.1. These alternating velocities are consistent with our interpretation of the features as eddies of CDW. Using the observed velocity fields and length scales of the features, we estimate *Ro*, the Rossby number of the features, to be 0.05–0.1, suggesting they are in geostrophic balance.

The observation of onshore flow in the central part of MT with off-shelf flow in the southwestern part of the trough has previously been noted from several years of Acoustic Doppler Current Profiler (ADCP) data collected on the Palmer Long-Term Ecological Research grid (Savidge & Amft, 2009). Such a circulation scheme was also reproduced in more recent modeling studies using both the 4 km and 1.5-km resolution model runs of ROMS (Dinniman et al., 2011; Graham et al., 2016). The circulation structure observed by the gliders is thus consistent with the schematic outlined in the water mass analysis, with mCDW cooled and modified by shelf processes being discharged at the southern side of the trough and being found over the bank. However, as shown in section 3.3, this does not imply that the southern side of the trough is the only source of shelf water—indeed, small cyclonic eddies of relatively cold mCDW are found much more widely on the shelf.

3.1.3. PV Fields

To investigate the dynamics of the flow in the vicinity of the bank and across the shelf break at the mouth of the trough, Ertel PV and its various terms were calculated, as outlined in section 2.2. In the analysis of the glider data, we approximate the lateral shear using the shear perpendicular to the glider profiles.

The total PV at different γ_n levels, the ratio of the lateral shear term to the stretching term (ζ/f), and the lateral gradient in PV, is shown in Figures 5 and 6, for Sections A and D, respectively. In the absence of frictional or diabatic processes, PV is conserved along streamlines. For Section A, which runs across the boundary current and onto the bank, the PV field is complex, but some clear patterns can be ascertained. First, the total PV (Figure 5a) for all neutral density layers denser than 27.7 kg/m^3 becomes more negative as one moves from the open ocean (unmixed CDW) onto the bank (mCDW), while density layers between 27.6 and 27.7 kg/m^3 exhibit a more modest increase in PV (Figures 5a and 5b). More negative PV is seen in the deeper layers over the bank as a result of the thinner isopycnal layers there; this coincides with the steering of the flow around the bank along f/H contours. However, this thinning does not occur in the near-surface layers (indeed note the thickening of the WW layer in Figure 2a); hence, $f\partial b/\partial z$ here is not strongly affected. On top of this general pattern, a more subtle inverted V-shaped pattern occurs in the PV field roughly 50 km along the baseline (Figure 5b), in association with the sharp velocity gradient separating the northeastward flowing boundary current from the westward flow over the bank itself (Figure 4a). This V-shaped feature stems from the lateral shear that separates these two features: ζ/f reaches −0.2 in this zone, enough to change the total PV by around 20% (Figure 5c). However, nowhere in the domain does ζ/f exceed −1 (Figure 5c); thus symmetric instabilities of the fluid are

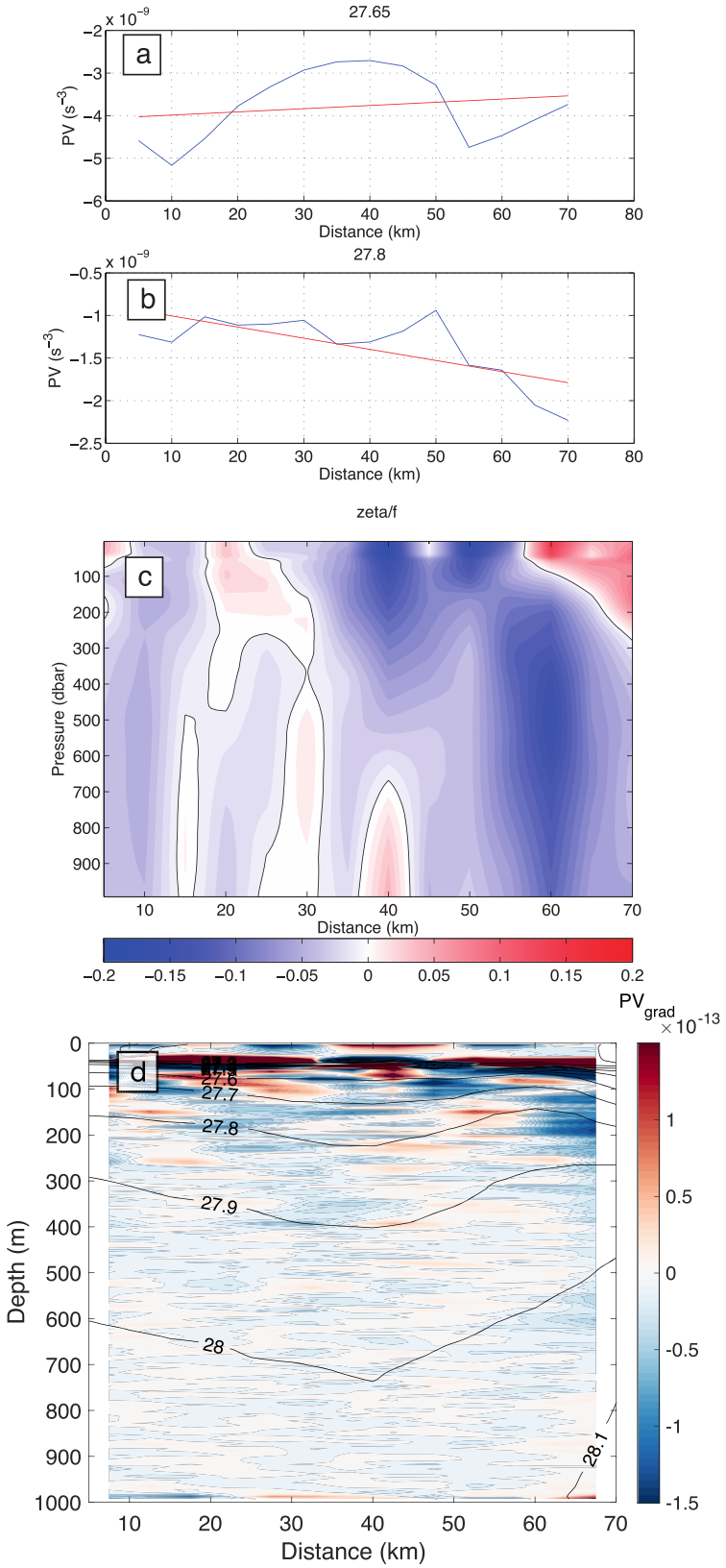

Figure 5. (a) Sections of PV (s^{-3}) along Section A, in the thermocline ($\gamma_n = 27.65$) and (b) at the top of the Circumpolar Deep Water layer ($\gamma_n = 27.8$ kg/m^3), with a linear fit to the trend in red. (c) Ratio of lateral shear term to stretching term (ζ/f) in the PV equation for Section A. (d) Lateral gradient in PV on Section A (s^{-3}/m). PV = potential vorticity.

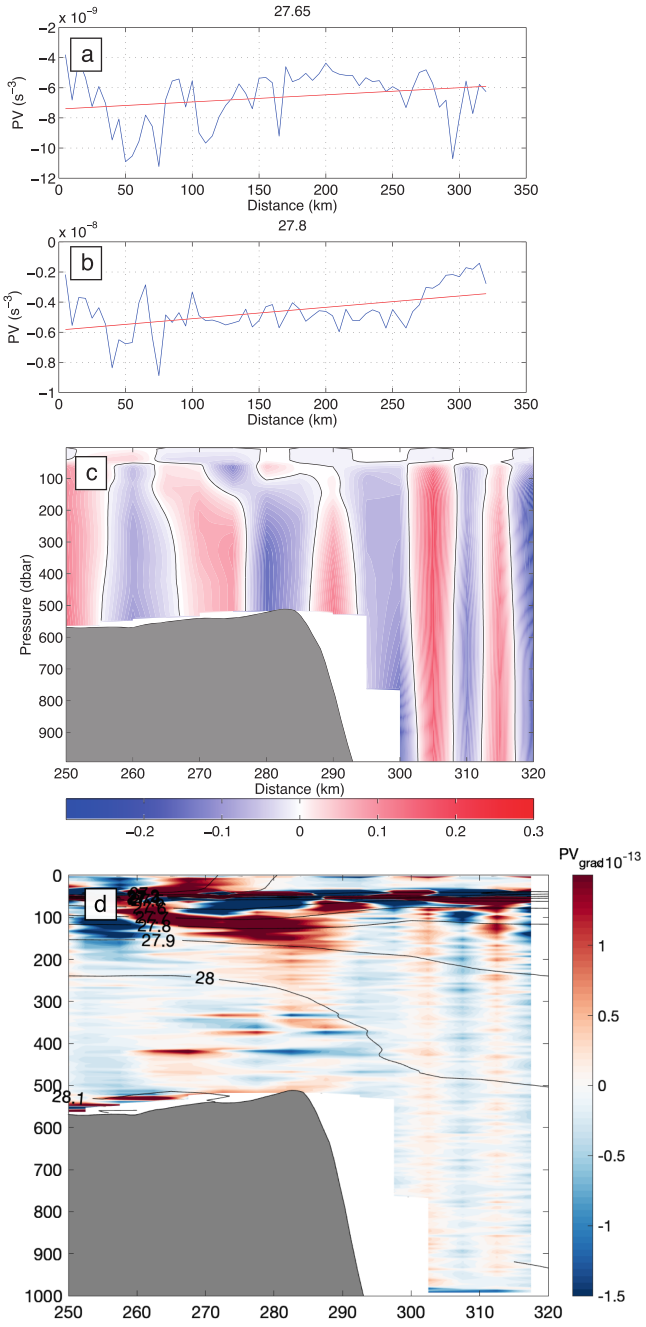

Figure 6. (a) As Figure 5 but for Section D.

unlikely to be active (Haine & Marshall, 1998). The lateral buoyancy term (not shown) is very small throughout the domain.

A similar pattern is exhibited by the PV field moving from offshore to onshore within MT along Section D, again across the observed streamlines (Figure 6). The total PV decreases moving onshore as a result of the thinning and shoaling of the individual layers (Figures 6a and 6b, such that shelf water of equivalent density has more negative PV than its offshore counterpart. In the case of the shelf waters, the reduction in PV also extends into lighter layers (Figure 6a). As previously discussed by Thompson et al. (2014), such downslope gradients in PV are conducive to an onshore eddy thickness flux of CDW onto the shelf. Once again, ζ makes a small but nonnegligible contribution to the total PV in the vicinity of the shelf break (up to 0.3 of the stretching term, Figure 6c). The water over the bank thus shares similar *T*, *S*, and *PV* characteristics to shelf water from outside the CDW eddies, and the observed circulation structure is consistent with the previous hydrographic observations indicating that the mCDW observed over the bank is of shelf origin.

Further insights about the likely stability of the boundary current can be gained from the cross-sectional gradients in the gridded PV fields PV_{grad} (Figures 5d and 6d). In previous studies (Hristova et al., 2014; Smith, 2007), horizontal changes in the sign of PV_{grad} have been shown to be conducive to barotropic instabilities being active, while vertical changes in the sign of PV_{grad} are one potential condition for linear baroclinic instabilities. There is evidence of these theoretical conditions being satisfied in Section A (Figure 5d). In the top 200 m, the criterion for baroclinic instability is satisfied, with clear vertical sign reversals around the WW layer and toward the top of the main thermocline at 50–200 m. By contrast, while gradients in the deep thermocline are weaker, there is evidence of horizontal PV sign reversals induced by the horizontal shear in the flow at 200–500 m. Similar conditions for both baroclinic and barotropic instabilities are found at the shelf break of Section D (Figure 6d, 270-290 km along the baseline). While suggestive of the boundary current being unstable around the mouth of MT, these measures are only snapshots in time and do not unequivocally demonstrate that these instabilities are present. In order to quantify more robustly the barotropic and baroclinic conversion of mean kinetic energy into eddies, the ROMS model is used to directly estimate these terms (section 3.3 below).

By way of summary of our glider results, Figure 7 displays the layer thickness of 27.9 kg/m^3 < γ_n < 28.0 kg/m^3, alongside the mean potential temperature in that density range, for Sections A and D. In both cases, the clear thinning of the CDW layer can be seen as one moves either onto the bank or over the shelf, with a corresponding cooling of the density layer as one encounters the mCDW. Temperatures are slightly cooler, and layer thicknesses slightly thinner, over the shelf compared with over the bank but taken together with evidence from Figures 2–6; the clear presence of shelf-derived mCDW over the bank can be detected.

3.2. Mean Circulation and Hydrographic Structure in MT and over the bank

3.2.1. Model Output

Key aspects of the observed hydrographic structure (Figures 2 and 3) are captured by the model and illustrated using properties averaged from January to March for both years (2008–2009) analyzed here. The plots (Figure 8) include the section running southwest to northeast across the bank (similar to glider Sections A and B) northwest to southeast (i.e., offshore to onshore) downstream of the bank (Section D) and a third section across the mouth of MT (similar to Section C; Figure 1b).

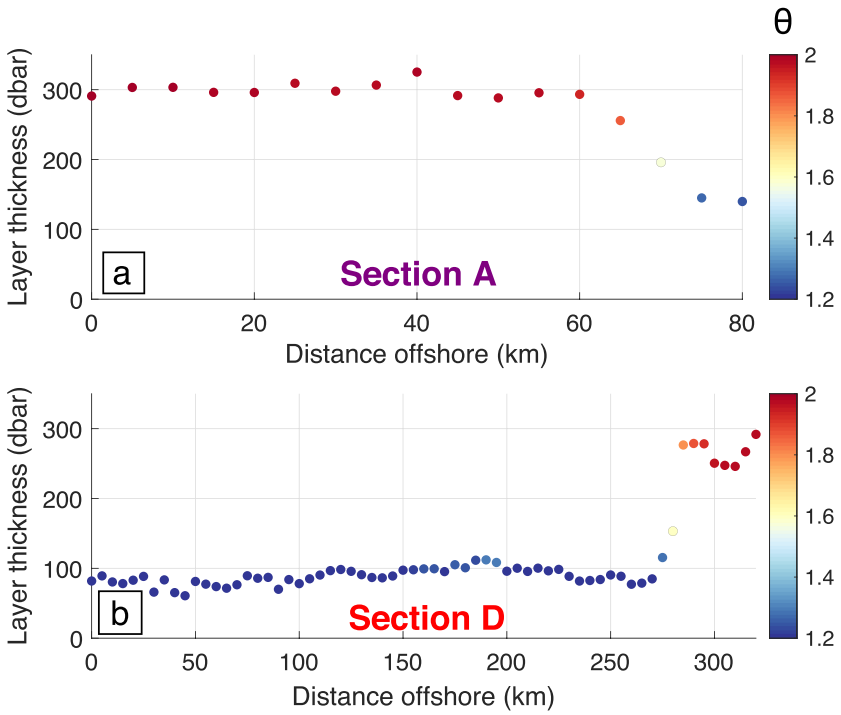

Figure 7. Circumpolar Deep Water (27.9 kg/m^3 < γ_n < 28.0 kg/m^3) layer thickness (dbar) and mean potential temperature (°C) along Sections (a) A and (b) D.

The cool water observed on the lee side of the bank is a fairly persistent hydrographic feature in the model. Below 200 m, isopycnals tend to shoal and thin over the bank as the CDW layer cools by around 0.2 °C (Figure 8a). Both north and south of the bank, the isopycnals deepen and thicken (the thickening is greater upstream of the bank). However, there is a systematic light bias (of around 0.2 kg/m^3) in the model compared with the observations in the deeper water masses; this occurs partly because the CDW in the model is fresher than the observations (Figure 8b).

The transition from open ocean to shelf structure is also well captured in the model. As in the observations, model Section D exhibits a thinning and shoaling of isopycnals moving offshore to onshore, with the unmixed CDW mainly confined to the off-shelf region (Figures 8e and 8f). Once again, the lower part of the water column is approximately 0.1–0.2 kg/m^3 less dense than in observations. Across the mouth of MT (Figures 8c and 8d), mCDW is found preferentially on the northern slope (60–80 km) of the trough, with colder waters along the southern bank. As expected from the long-term averaging of the model field, the model section does not show the same level of small-scale mesoscale variability as the glider section. However, both models and observations (Figures 2c and 2f) support previous work indicating that the northern bank of MT is a preferred pathway for onshore heat transport across the shelf.

As in the observations, PV in the deeper layers becomes more negative both over the bank and moving from the offshore open ocean to the onshore trough region as one crosses the streamlines of the flow (not shown). This reduction in PV occurs primarily due to the squeezing of the isopycnals in the deeper layers, which decreases the stretching term. In contrast, and in common with the observations (Figure 4), the near-surface layers show a slight reduction in the magnitude of negative PV due to a decrease in the stratification of the near-surface waters. The gradients in PV, conducive to baroclinic instability being present in the near-surface layers and barotropic instabilities below 200 m, are also well reproduced (Figures 9a, 9c, and 9e). ζ/f is also very similar in magnitude (0.2–0.3, Figures 9b, 9d, and 9f) suggesting that the model is successfully capturing the dynamics seen in the observations. The similarity in results between the model and the observations also suggests that the error incurred in the observational PV estimates by only including one horizontal component of the horizontal shear and buoyancy terms is small.

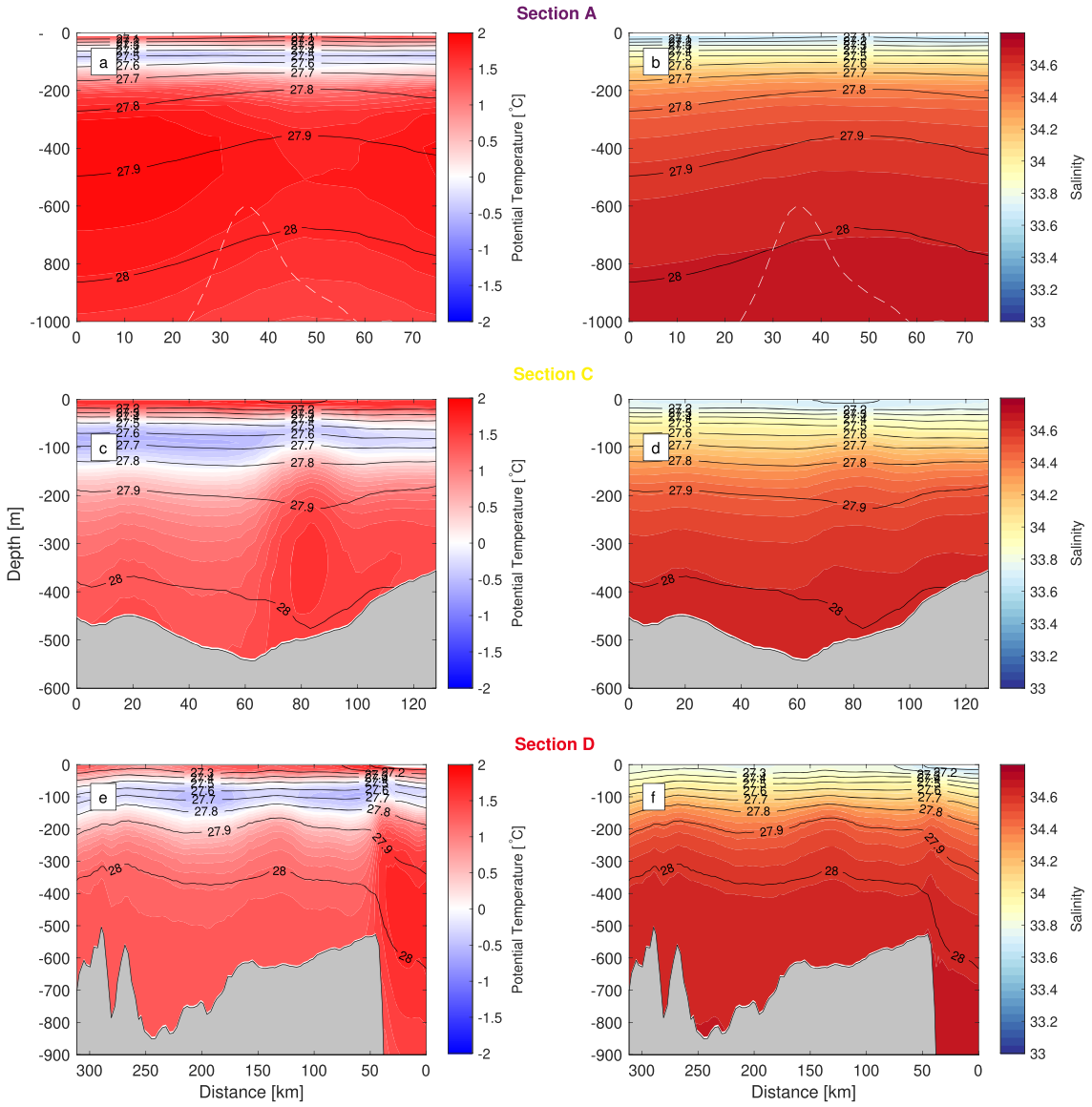

Figure 8. Summer-averaged (January–March) potential temperature (a, c, and e), salinity (b, d, and f), and neutral density (all panels, black contours) computed from the 2008–2009 model output. The dashed line in panels a and b shows the bathymetry (i.e., the bank) shifted upward 2,200 m. Notice that the section labeled "A" aims to illustrate the hydrographic structure crossing the bank and does not match exactly the glider survey. The location of the sections is shown in Figure 1.

A plan view of the circulation around MT and the slope bank (Figure 10) helps clarify the strong influence that these topographic features have on the deep circulation. The figure shows the temperature and horizontal velocity from the model output, vertically integrated between 27.8 kg/m^3 < γ_n < 28.0 kg/m^3, and averaged for summer (January to March) as in Figures 8 and 9. Figure 10a shows strong slope flow bifurcating into two branches as it encounters MT and the bank. The outer branch moves offshore around the bank, forming a large recirculating eddy off its tip, with some of the flow returning to the slope downstream of the bank. The inner branch moves onshore as it encounters the MT. This accelerated circulation leads to shoaling of the isopycnals (not shown) and thinning of the layer over the bank and within the eddy (Figure 10a). Cold anomalies are also evident over the bank, which we argue is being exported from the shelf by both the mean flow and eddy features generated at the slope.

3.2.2. Altimetry

The impact of the bank on the circulation found with the model is also evident in satellite altimetry and derived surface geostrophic currents. The mean field is displayed in Figure 11a. A strong gradient in SSH

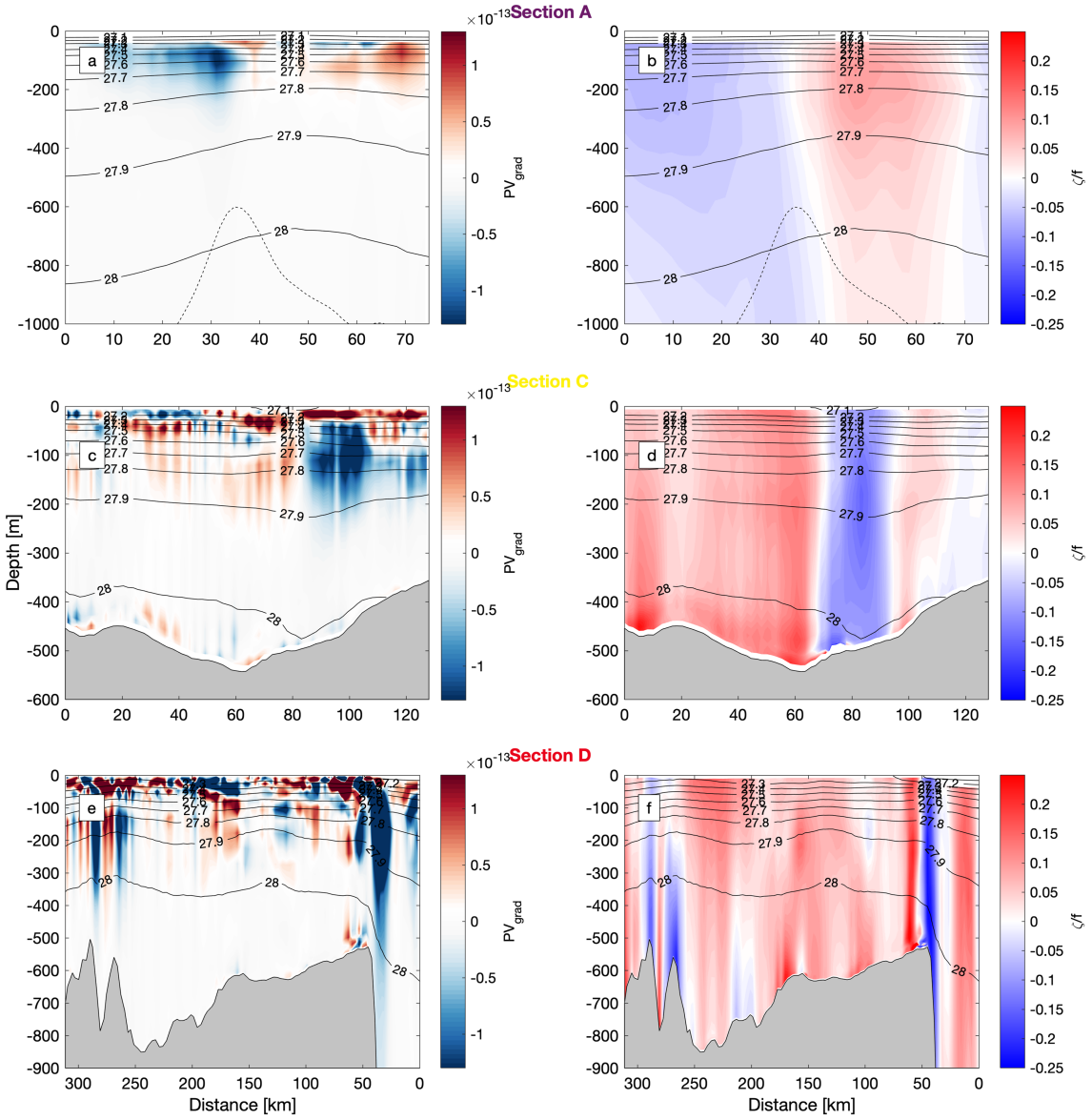

Figure 9. Summer-averaged cross-section potential vorticity gradients (a, c, e) and ratio of relative to potential vorticity (b, d, f) computed from the model output. Section locations were chosen to approximately match the glider surveys and are shown in Figure 1.

is aligned along the shelf break separating the offshore ACC water masses from the on-shelf water masses. This strong gradient denotes the position of the southern boundary of the ACC. However, the location of the front is strongly guided by the topography of the shelf break, and a significant offshore meander in the front occurs at the location of the bank, with low dynamic height water being found up to 150 km offshore of the main continental slope. The standard deviation in dynamic height (Figure 11b) reveals a local minimum around the shelf break itself indicating that the front is relatively stable in its position over the 24 years. Much stronger variability is observed further offshore owing to the eddy-rich field of the ACC, and also, to a lesser degree, over the continental shelf itself. However, there is also a region of much stronger SSH variability (2–3 times the variability over the continental slope) just to the north of the bank, around 65°S, 73°W. This is the signature of the large cold-cored recirculating eddy seen in the model field in section 3.2.1. Inspection of the monthly fields (not shown) reveals that the position of this eddy, and whether it forms closed contours or is meander-like in appearance (e.g., as Figure 11), varies, explaining the enhanced variability in SSH. At the time of the glider occupation (Figure 11c), a large cyclonic tip eddy is centered at 65.5°S, 73°W, and it is clear that the observations (section 3.1) sampled the inner edge

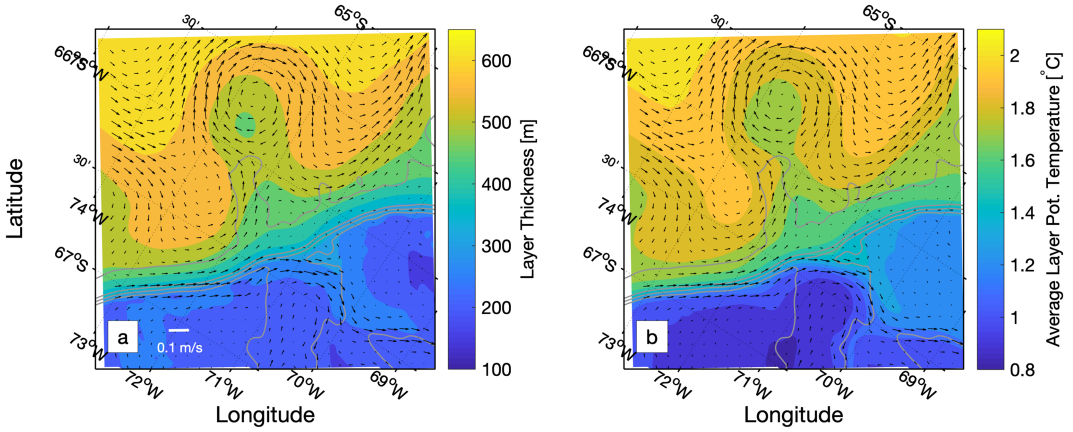

Figure 10. Time-mean properties and horizontal circulation vertically averaged between neutral density surfaces $\gamma = 27.8$ and $\gamma = 28$ kg/m^3. The left panel (a) shows the average layer thickness, and the right panel (b) shows the average θ for the layer.

of this eddy over the bank itself. Further information pertaining to the variability of the SSH field is discussed in section 4.

With the model fields successfully reproducing key elements of the hydrography and the circulation observed both in the glider surveys and satellite observations, we use its 2-year run to investigate the mechanisms of export of cold mCDW from the shelf and discuss the impact these processes have on WAP dynamics.

3.3. Eddy-Mediated Export of Shelf Water

The presence of a significant volume of cold mCDW over the bank revealed by the off-shelf glider survey raises the question of how this water is exported and what role the bank and MT play in this process. Examination of the model output revealed frequent, small, cold, eddy-like events at or near the edge of the shelf, which then carried cold water offshore. Weekly snapshots of θ and circulation at 300 m from the model output (Figure 12) provides an example of such events. On 25 October 2009 (Figure 12b), an eddy can be seen just on top of the bank, embedded within one of two cold filaments originating from the shelf and carried by flow moving offshore as it navigates around the bank. On 1 November (Figure 12c), a pair of new cyclonic, cold-core eddies form both upstream and downstream of MT, associated with strong velocity shears. In subsequent snapshots (Figures 12d and 12e), the upstream eddy is advected over the bank, following the eddy from 25 October, while the downstream one is advected away along the shelf. The bank eddies contribute to cooling both over the bank and appear to dissipate into the larger-scale cold anomaly formed by the much larger, persistent cyclonic feature found off the tip of the bank. The structure and variability of this larger feature is discussed further in section 4.

Identifying, tracking, and characterizing these individual eddies from observations or model output can be done in a number of ways, including by finding closed contours of SSHA, PV anomalies, or anomalies of hydrographic properties (Chelton et al., 2011; Chelton et al., 2011). Eddies on the WAP shelf have been characterized with both hydrographic surveys and moored time series using temperature anomalies and velocity records, when available (Couto et al., 2017; Martinson & McKee, 2012 ; Moffat et al., 2009). Both these methods require making assumptions about the shape of the eddies. To avoid defining the eddy temperature anomalies a priori or mistaking isolated eddies for filaments or other cold-water intrusions on the bank, we use the velocity field at 300 m to identify the eddies. In particular, we use the second invariant of the velocity gradient tensor (Isern-Fontanet et al., 2003; Kurian et al., 2011):

$$\Phi = -\left(\frac{\partial u}{\partial x}\right)^2 - \left(\frac{\partial v}{\partial x}\right)\left(\frac{\partial u}{\partial y}\right) \tag{2}$$

When positive, Φ indicates motion dominated by rotation over deformation, and closed contours of Φ can be used as a proxy for the presence of eddies (Kurian et al., 2011). The value of the isoline to identify and track

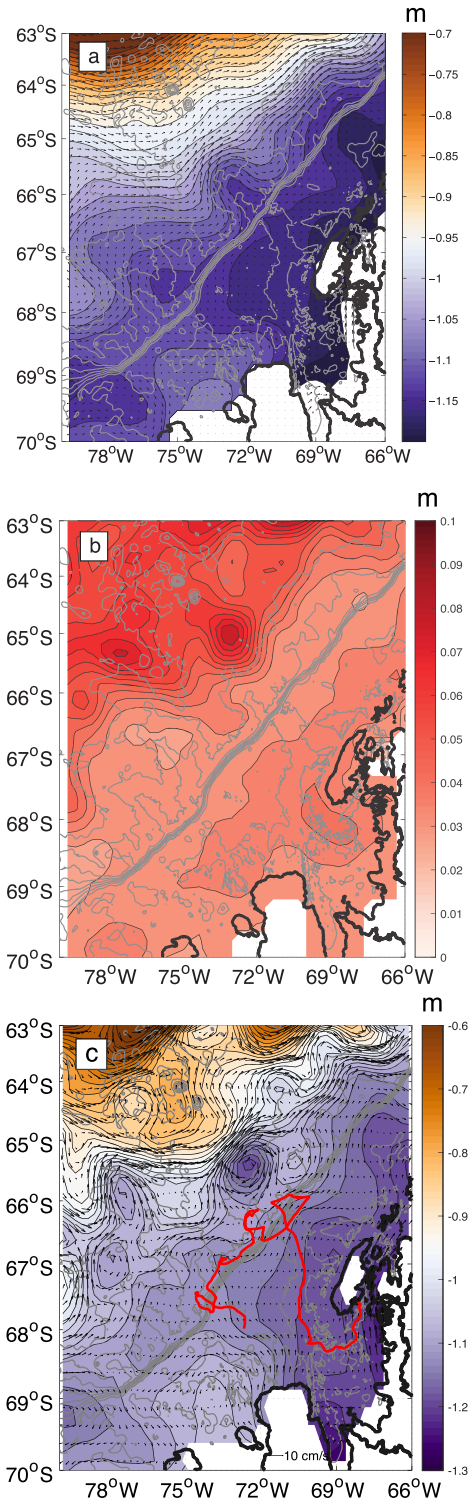

Figure 11. (a) Mean sea surface height (SSH) for 1993–2016 (in dyn. m), from AVISO (1/4)° satellite altimetry. IBCSO bathymetry at 500-m intervals to 4,000 m is shown in gray, and mean geostrophic velocities are shown with black arrows. (b) Standard deviation of SSH anomaly for 1993–2016. Note the high standard deviation region just north of the bank, around 65°S, 73°W. (c) SSH and surface geostrophic velocity field at the nearest weekly time step to the glider occupation, dated 15 February 2015. The glider track is overlain.

eddies used here is 10^{-10} s^{-2}, which provided reliable identification of cold-anomaly features identified visually on the model output. Once closed contours of the isoline are selected, a handful of tests are applied to select the final data set. First, a shape test selects for closed contours that do not deviate from a circular shape by a given shape error, expressed by the ratio of the sum of the areas of the closed contour that deviate from a perfect circle divided by the area of the perfect circle itself. A minimum value of 75% is required for identification. Larger values would result in more eddies being identified but at the cost of accepting increasingly irregularly shaped features. A second test requires the radius of the fit shape to be at least 3 km given the model resolution of 1.5 km. Once identified, mean relative vorticity, mean potential temperature, and size are computed for each eddy defined by the closed contour. Eddies identified in individual model snapshots are followed as the analysis moves forward in time by searching a region roughly twice the size of the eddy in the following snapshot. If more than one eddy is found in that region, the eddy closest in size is selected. Finding each eddy is attempted for 3 days into the future, and if the search fails, the event is considered terminated. While we attempted to ensure that these results are not very sensitive to method parameters, the fact is we are tracking these small eddies very near their formation region and they are easily deformed and dissipated through interactions with the larger-scale flow. This could result in miscounting eddies that, for example, become temporarily deformed (i.e., failing the shape test) while largely retaining their hydrographic signature. However, the analysis still provides valuable information about the characteristics of the eddy population. Later in the paper, and to sidestep these issues, we discuss more generally the role of transient heat fluxes, which include the coherent eddies described here.

The bottom panels of Figure 12 show the evolution of the Φ field during the eddy generation events discussed above using the θ and velocity fields at 300 m, and they capture the structure and evolution of the eddies. The cold, cyclonic features are associated with strong maxima in Φ and show both the eddies upstream of the bank being advected toward the larger eddy off the tip of the bank and a third forming just downstream of MT and being advected alongshore.

Applied to 2 years of model output, the above methodology found 86 eddies that passed over a region centered over the bank bounded by the 2,600-m isobath (about midslope) and extending about 80 km along and 55 km away from it (box in Figure 15). Of those, 65 eddies were cyclonic (Figure 13a), with the vast majority (85%) of cyclonic eddies having temperatures lower than 1.5 °C (with a mean of 1.37 °C, Figure 13b), a typical temperature used to distinguish modified UCDW (Moffat et al., 2009). The median and mean radius of cyclonic eddies on the bank was 6.0 and 6.2 km (Figure 13c), respectively, which is largely consistent with the warm, anticyclonic, UCDW-core eddies found on the shelf (e.g., Martinson & McKee, 2012 ; Moffat et al., 2009) and rather smaller than the open ocean eddies typically found in Southern Ocean surveys. Note also that two to three warm eddies are evident on the northern bank of MT over this roughly 1-month period, which is consistent with the 35 to 45 eddies per year identified in this region with moored time series (Martinson & McKee, 2012; Moffat et al., 2009). Measures of the lifespan of the eddies on the region around the bank suggest mean time scales of about 10 days (Figure 13d), although these findings should be

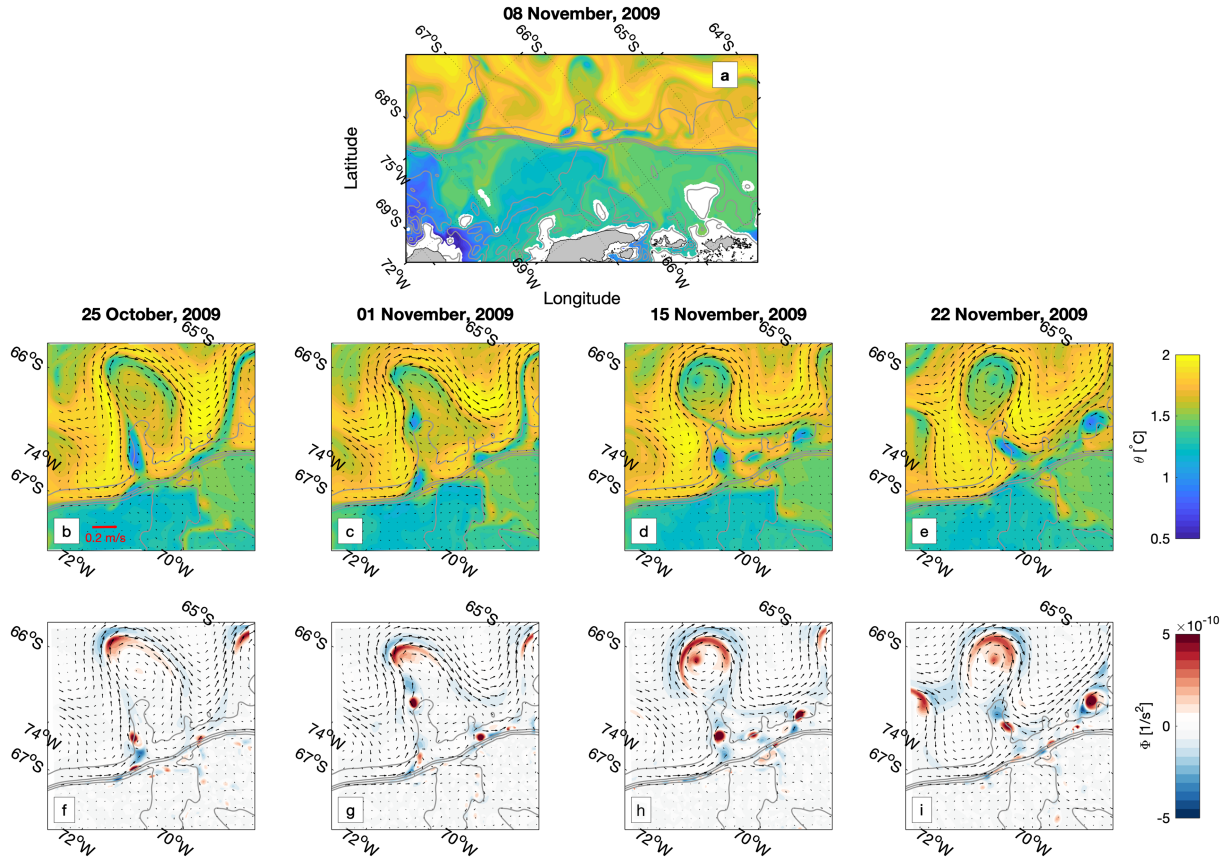

Figure 12. Model snapshots at 300-m depth showing the export of cold shelf water by eddies and filaments. Panel (a) shows the broad-scale distribution of potential temperature during the middle of the period considered. Panels (b) to (e) show weekly snapshots of potential temperature over a 1-month period. Panels (f) to (i) show the distribution of Φ calculated from equation (2). In all panels, bathymetric contours (250, 500, 700, 1,000, and 3,000 m) are shown as gray contours. Blank regions on the shelf on panel (a) are shallower than 300 m.

interpreted cautiously: Eddies that deform past the standard for identification will be removed from the count, but the associated hydrographic anomalies might still be present in the water column. These findings reinforce the idea that these eddies are generated on the shelf, carry cold shelf water by the slope currents onto the bank where at least part of their water is entrained into the larger tip eddy.

Eddies such as those shown in Figure 12 are the result of instabilities extracting energy from the mean flow. Using the model output, we calculated the baroclinic conversion rate $-\overline{\rho' w'}$, which is associated with baroclinic instabilities and the barotropic conversion rate $-\rho_0\left(\overline{u'u'}U_x + \overline{u'v'}U_y + \overline{v'u'}V_x + \overline{v'v'}V_y\right)$ which is associated with barotropic instability (e.g., Hristova et al., 2014; Wallace & Lau, 1985). In these expressions, all variables have been decomposed as, for example, $u = U+u'$, so that (U,V) and (u',v') are the time-mean and time-varying components of the horizontal velocities, and ρ' and w' are the time-varying density and vertical velocity, respectively. The overbar indicates that the variables have been time averaged. Figure 14 shows the barotropic and baroclinic conversion rates integrated from 150 to 700 m, chosen to examine eddy generation in the subsurface layer where cold shelf water is found. As suggested by the PV gradients from both observations and the model results, barotropic and baroclinic instability appear significant in the study region, albeit with distinct spatial patterns. While both baroclinic and barotropic instability are active on the open ocean, the former is suppressed along the strongly sloping bottom of the shelf break, a result expected from a theoretical analysis of this problem (Isachsen, 2011; Smith, 2007). Barotropic instability appears dominant on the slope around the bank and the northern bank of MT, the latter a well-understood region of high eddy activity on the shelf (Martinson & McKee, 2012; Moffat et al., 2009). This spatial pattern is consistent with the strong lateral shears that the flow develops as it bifurcates first into the offshore branch along the bank and a shoreward branch moving into MT.

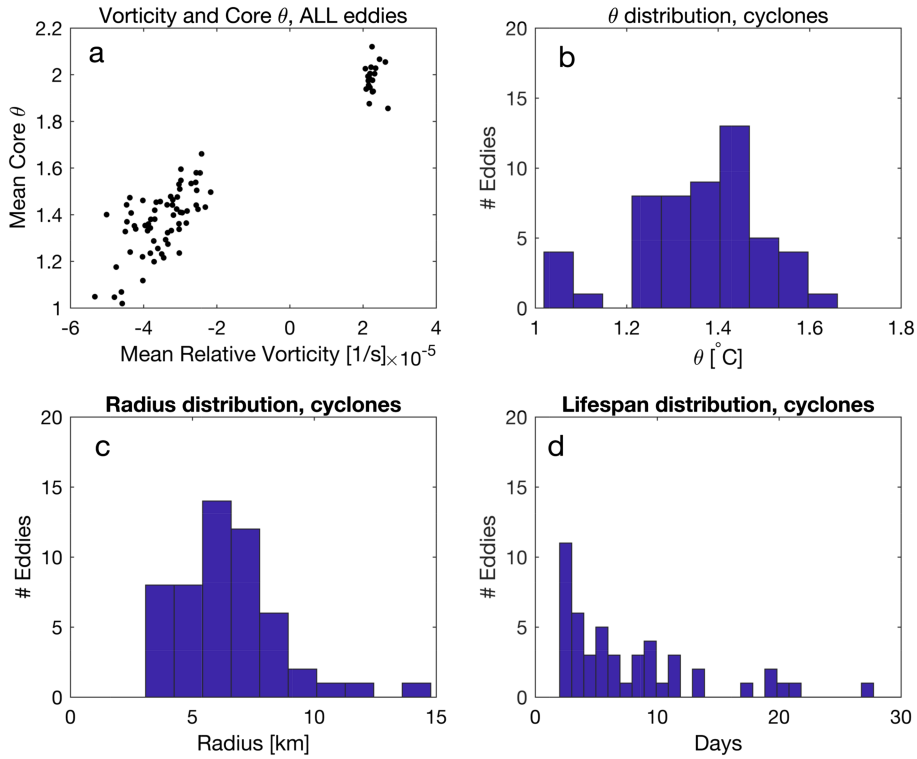

Figure 13. Summary characteristics of 86 unique eddies found over the bank (the region is shown in Figure 15) at some point during the 2-year model run. Panel (a) shows the relative vorticity (cyclonic is <0) against average core temperature at 300 m, (b) the frequency of cyclones by temperature class, (c) the frequency of cyclones by radius class, and (d) the frequency of cyclones by lifespan in days.

The instability of the shelf edge flows appears to lead to significant export of the colder mCDW and thus contributes to the warming of the shelf by the eddy heat fluxes. To illustrate this export and its variability, we use the model output to examine the evolution of both θ and the eddy flux contribution to the heat budget $-\nabla_h \cdot \left(\overrightarrow{u'}\, T'\right)$, where, as described above, prime variables represent the time-varying component and $\overrightarrow{u}$ is the horizontal velocity. Again, we focus on the subsurface layer by averaging the temperature and vertically integrating the eddy heat fluxes from 150 to 700 m, where cold water from the shelf is observed. To provide a

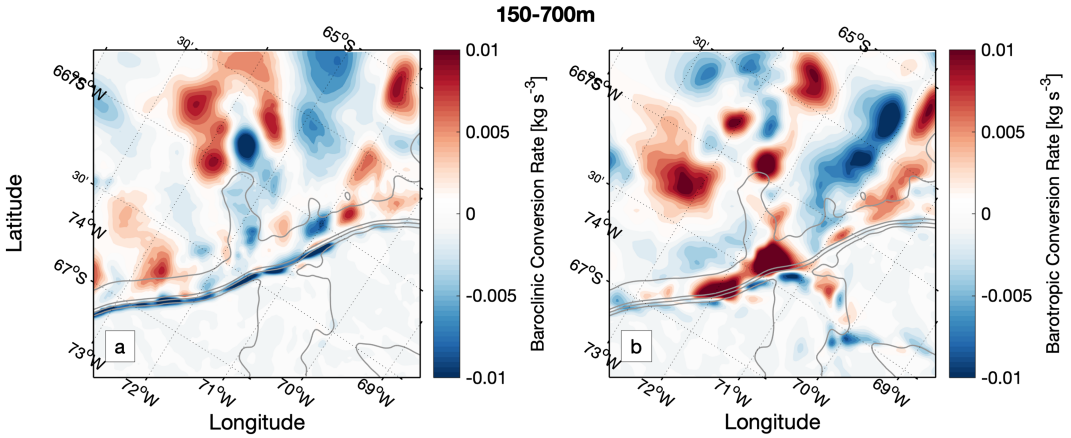

Figure 14. Baroclinic (panel a) and barotropic (panel b) energy conversion rates (defined in section 3.3) time averaged for the 2-year model run and vertically integrated from 150 to 700 m.

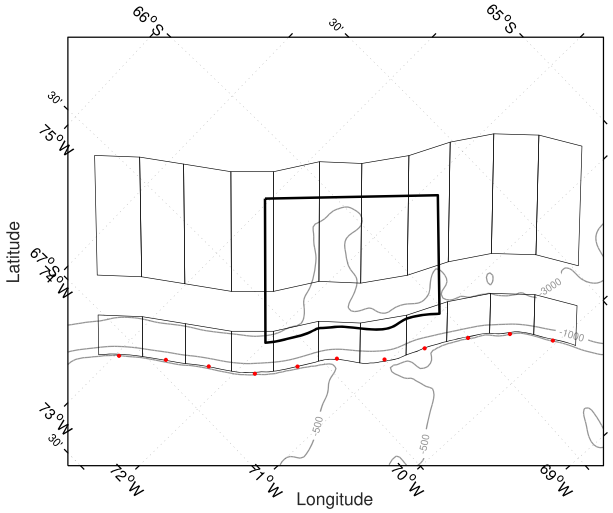

Figure 15. Grid used to average the potential temperature and eddy heat flux divergence shown in Figures 16 and 17. Distance increases left to right (southwest to northeast). Selected isobaths show the model bathymetry, with the bank outlined by the 3,000-m contour. The region used to characterize the eddy population over the bank (Figure 13) is outlined by the thick black line.

contrast between the region where the export is originating near the shelf, and the open ocean, we further area average the model output onto two different grids: one along the shelf slope and a second, parallel to the first, farther offshore (Figure 15).

Along the slope, frequent, relatively cold, eddy-like events ($\theta < 1.5$ °C) are evident throughout the 2-year model run we analyzed (Figure 16a). These cold events are generally associated with the highest eddy heat fluxes in the record. While many of the events appear to originate upstream of the bank (e.g., left of the two vertical lines indicating the approximate position of the front), such as the one discussed above (Figure 12), southwestward (i.e., right to left) propagation is also common, indicating that these shelf slope eddies are effective at exporting cold shelf water along the entire study region. While the mean circulation would appear to favor northeastward (left-to-right) advection of the eddies, frequent weakening or reversal of the alongshore low-frequency flow allows for this upstream propagation of the eddies along the slope. On average, the eddy heat fluxes lead to cooling over the region of the slope around the bank (Figures 16c and 16d).

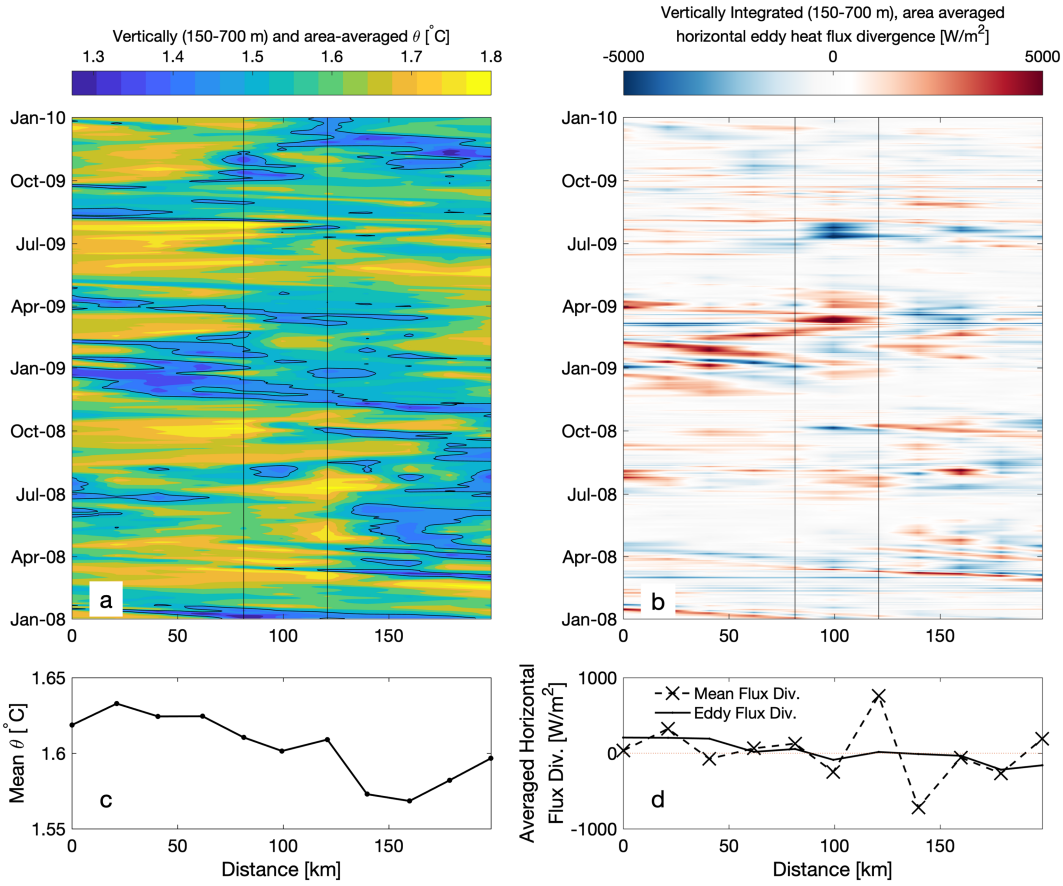

Figure 16. Time variability of the vertically averaged (150–700 m) potential temperature (panel (a)) and vertically integrated (same depth range) horizontal component of the eddy heat flux divergence term $-\nabla_h \cdot \left(\overline{\vec{u}'T'}\right)$, where negative values indicate cooling (panel b). The variables are further area averaged onto a grid along the continental slope, shown in Figure 15. Panels (c) and (d) show the same variables but time averaged for the entire records. Panel (d) additionally shows the horizontal component of the mean heat flux divergence term $-\nabla_h \cdot \left(\overline{\vec{u}}\,\overline{T}\right)$.

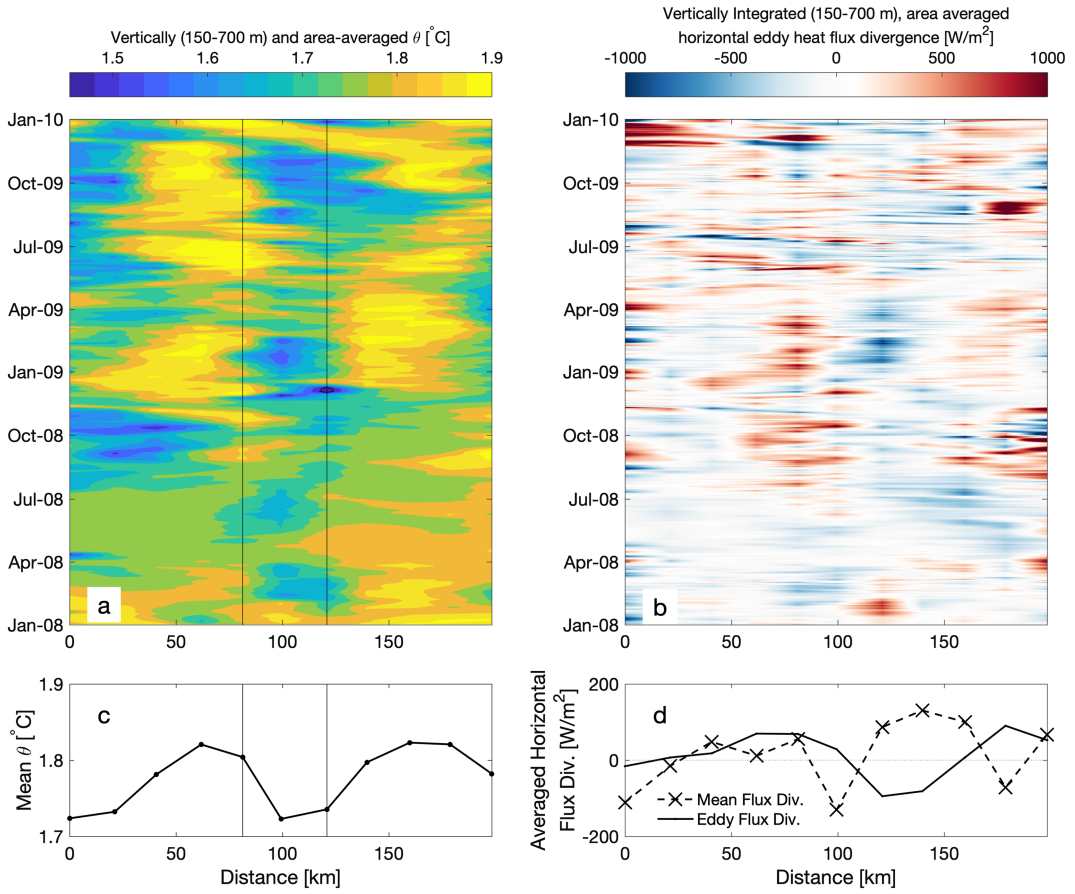

Figure 17. As Figure 16 but variables are gridded using the offshore grid in Figure 15.

The model results along the offshore grid show the persistent presence of cold water and corresponding eddy-driven cooling around the bank (Figures 17a and 17b). This is consistent with the bank acting both as pathway for the offshore transport of the slope eddies discussed above and also as a retention mechanism for cold water (Figure 10) by encouraging the formation of a persistent, larger eddy off the tip of the bank, a feature that was observed in altimetry records (Figure 11c) as well as reproduced in the model. This persistence is also reflected in the spatial and temporal structure depicted in Figures 17a and 17b, with spatial scales of several tens of kilometers, consistent with a large topographic eddy at the tip of the bank, and eddy fluxes that generate cooling for several months at a time. This is in strong contrast with the rapid propagation of relatively small eddy events along the slope. On average, and as shown in Figures 10b, 17c, and 17d, this eddy-driven cooling helps explain the colder temperatures that are commonly found on the bank and observed by the glider surveys.

Overall, analyses of the observations and model output suggest the interaction between the ACC flow along the slope and the complex shelf and slope bathymetry is critical to understand the export of cold mCDW from the west Antarctica Peninsula shelf. Relatively small cyclonic cold eddies are generated along the slope, and this generation appears to be enhanced around MT and the slope bank, which force the flow to bifurcate and generate favorable conditions for flow instabilities. The flow around the bank results in the formation of a much larger, persistent cyclonic eddy, which suggests a cascading of eddy energy toward larger scales from the shelf slope to the surrounding open ocean, to where this cold water is ultimately exported.

4. Discussion

This section addresses two remaining questions pertaining to the export of this mCDW. First, how does water transported onto the bank and captured within the large tip eddy migrate into the interior? Second,

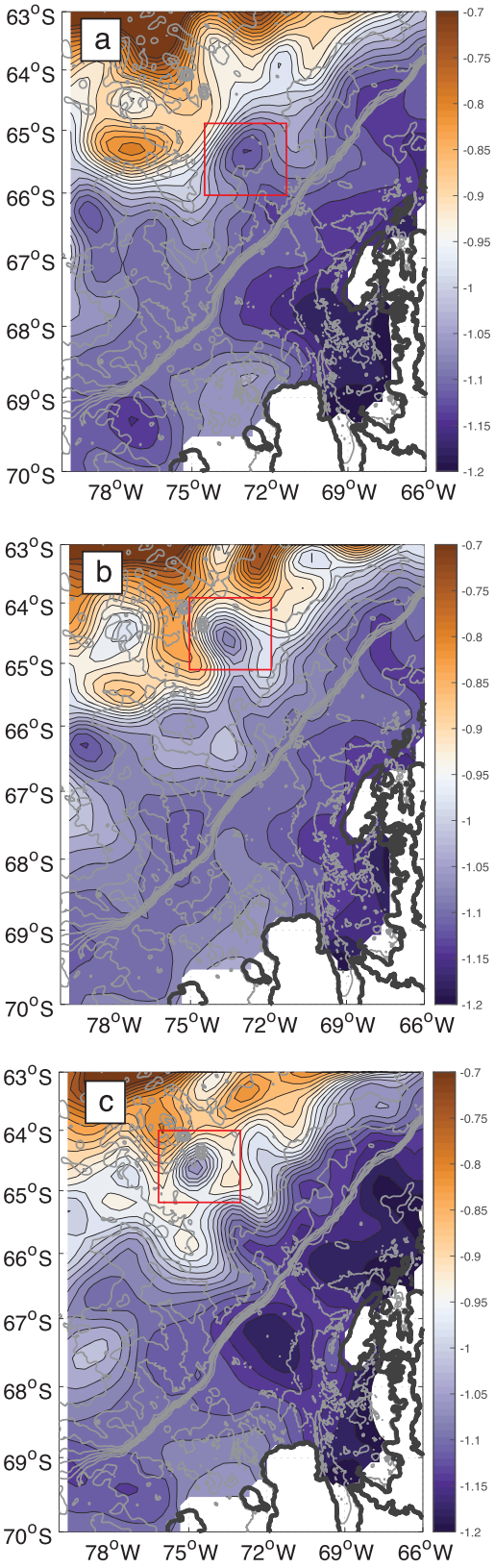

Figure 18. Monthly mean sea surface height fields (and bathymetry), as in Figure 9a, from (a) April 2010, (b) May 2010, and (c) June 2010, showing a large cyclonic eddy (outlined in red) detaching from the boundary current.

what implications does this have for export of shelf waters more widely from the Antarctic Peninsula shelf? This paper does not aim to answer these questions fully but to provide avenues for future investigation.

4.1. Possible Fate of Shelf Water

It was noted in section 3.2, from both modeling and altimetry, that large eddies have a tendency to sit at the tip of the bank and that this is a region of enhanced SSH variability (Figure 11c). The mean diameter of these eddies was calculated from altimetry to be 116 ± 6 km, and their typical Rossby numbers are 0.06 ± 0.004 (the errors represent a standard error on the estimates). To investigate more closely the cause of the enhanced SSH variability, each individual monthly snapshot of SSH and geostrophic velocity from altimetry was investigated. From this study, and using the methodology outlined in section 2.4, closed cyclonic contours of SSH were identified in 60% of the monthly means, implying that the tip eddy forms regularly from the meander as the boundary current is steered around the bank (note that if multiple instances of closed contours are observed in monthly snapshots, this is simply counted as one eddy present). Within the 24-year period, there are also 31 occasions where the large tip eddy appears to detach from the boundary current, propagating either northward into the ACC or northeastward with the boundary current. After the detachment, the eddy then appears to decay as it moves toward the ACC, rapidly losing its identity. An example of this detachment can be found in Figure 18 in April to June 2010, but other notable examples occur in, for example, November 2011 and June 2012. Such detachment events may therefore be implicated in the final movement of mCDW into the interior of the Southern Ocean, though the altimetry lacks sufficient horizontal resolution to determine the total magnitude of this volume/buoyancy flux associated with this process or whether eddies or filaments smaller than can be observed using satellite altimetry are also responsible for fluxing mCDW into the Southern Ocean interior.

4.2. Implications for Ocean-Shelf Exchange in the West Antarctic

This study has identified an important route by which cold deep waters are exported from the WAP shelf and a potential mechanism moving eddies of this water mass into the Southern Ocean interior. While this study has focused on one prominent trough (MT), large glacially carved features such as this are common elsewhere on the peninsula (e.g., Belgica Trough to the south and Palmer Deep Trough to the north). Furthermore, Hillenbrand et al. (2008) document at least eight such drift features similar to the topographic bank we have described on the continental slope of the Bellingshausen Sea. It is therefore expected that the processes documented here occur more widely than in the restricted geographical domain we have studied.

While the eddy heat flux across the shelf break was quantified in section 3.3, there remain two key challenges to understanding the role of the mechanism outlined to the West Antarctic more generally. First, more observations are required both around the mouth of MT and also around other similar canyons, to identify the ubiquity or otherwise of both the large tip eddies and the smaller cold-cored cyclonic eddies elsewhere on the continental slope. Once this issue is addressed, the high-resolution model can then be used to quantify the boundary current to open ocean fluxes elsewhere on the shelf. This process should reduce some of the existing large uncertainty in eddy heat flux estimates for the WAP.

5. Conclusions

Using a unique high-resolution glider data set, satellite altimetry and a 1.5-km model run, a new pathway and likely mechanism for the export of deep West Antarctic shelf waters to the Southern Ocean has been outlined. Ocean glider data from close to the mouth of a large glacially carved trough has revealed a region of low PV water near the shelf break, with *T/S* characteristics akin to deep waters observed on the inner shelf. These shelf-derived waters are located over a topographic bank at the mouth of MT which, through the need to conserve PV, directs the boundary current around it and acts as a retention area for this water. Subsequent examination of a high-resolution model suggests that shelf waters are brought onto the bank by small (6 km) cyclonic eddies shed from the boundary current, which generally last ~10 days before losing their identity. These eddies tend to cool the larger (116 km) tip eddy that exists commonly over the bank, with both the observations and modeling suggesting that barotropic instability is implicated in the conversion to eddy kinetic energy. The ultimate fate of these waters has not been fully resolved, but analysis of 24 years of altimetry suggests that detachment events of the large eddy regularly take place, though we are unable to determine whether smaller eddies or filaments also detach and move into the Southern Ocean interior.

While much research focus has been directed toward the eddy flux of heat from the UCDW onto the shelves of the West Antarctic, understanding the offshore export of waters with cooler than average deep temperatures is vital to quantifying the onshore heat transport with confidence. This is a significant problem, as several studies have pointed to an increased volume flux of warm CDW onto the West Antarctic shelves as leading order mechanism for the increased recession rates of ice shelves and glaciers in this region in the 21st century (Cook et al., 2016; Schmidtko et al., 2014). Furthermore, the relationship between these cold-cored eddies and their warm counterparts that are the main driver of this eddy heat flux remains to be fully understood.

Nevertheless, the ubiquity both of deep topographic troughs such as MT and the presence of several topographic banks at the shelf edge of the northern part of the peninsula imply that the processes identified in this study may be important in setting the overall cross-shelf break heat flux.

Acknowledgments

The authors thank Dr. Jennifer Graham for her extensive work in setting up and testing the ROMS 1.5-km model for the West Antarctic Peninsula. The work was supported by NERC Independent Research Fellowship NE/L011166/1 and NSF Grants 1703310 (C. Moffat) and 1543018 (M. Dinniman). We also thank the officers and crew of *RRS James Clark Ross* and *RV Lawrence M. Gould*. The altimeter products were produced by Ssalto/Duacs and distributed by Aviso, with support from CNES (2011) and can be found online (https://www.aviso.altimetry.fr/en/data/data-access/gridded-data-extraction-tool.html). The glider data (temperature, salinity, pressure, and velocity fields) are uploaded with this submission in Matlab format (data_final_409_agu.mat), and the Antarctic Peninsula velocities used to detide the glider data can be found online (https://www.esr.org/polar_tide_models/Model_AntPen0401.html). Model fields from the ROMS output can be found online (https://odu.box.com/s/kq0r6epdz6akxvgtkemyigxyd0cyslz6). We additionally thank two anonymous reviewers for their helpful comments on the manuscript.

References

Arndt, J. E., Schenke, H. W., Jakobsson, M., Nitsche, F. O., Buys, G., Goleby, B., et al. (2013). The International Bathymetric Chart of the Southern Ocean (IBCSO) version 1.0—A new bathymetric compilation covering circum-Antarctic waters. *Geophysical Research Letters*, *40*, 3111–3117. https://doi.org/10.1002/grl.50413

Bers, V., Momo, F., Schloss, I., & Abele, D. (2013). Analysis of trends and sudden changes in long-term environmental data from King George Island (Antarctica): Relationships between global climatic oscillations and local system response (Vol. 116). https://doi.org/10.1007/s10584-012-0523-4

Brearley, J. A., Pickart, R. S., Valdimarsson, H., Jonsson, S., Schmitt, R. W., & Haine, T. W. N. (2012). The East Greenland boundary current system south of Denmark Strait. *Deep-Sea Research Part I-Oceanographic Research Papers*, *63*, 1–19. https://doi.org/10.1016/j.dsr.2012.01.001

Budgell, W. P. (2005). Numerical simulation of ice-ocean variability in the Barents Sea region. *Ocean Dynamics*, *55*(3), 370–387. https://doi.org/10.1007/s10236-005-0008-3

Callahan, J. E. (1972). The structure and circulation of deep water in the Antarctic. *Deep Sea Research and Oceanographic Abstracts*, *19*(8), 563–575. https://doi.org/10.1016/0011-7471(72)90040-X

Carton, J. A., & Giese, B. S. (2008). A reanalysis of ocean climate using simple ocean data assimilation (SODA). *Monthly Weather Review*, *136*(8), 2999–3017. https://doi.org/10.1175/2007MWR1978.1

Cenedese, C., & Linden, P. F. (2002). Stability of a buoyancy-driven coastal current at the shelf break. *Journal of Fluid Mechanics*, *452*, 97–121. https://doi.org/10.1017/S0022112001006668

Charney, J. G. (1947). The dyanmics of long waves in a baroclinic westerly current. *Journal of Meteorology*, *4*, 135–162.

Chelton, D. B., Gaube, P., Schlax, M. G., Early, J. J., & Samelson, R. M. (2011). The influence of nonlinear mesoscale eddies on near-surface oceanic chlorophyll. *Science*, *334*(6054), 328–332. https://doi.org/10.1126/science.1208897

Chelton, D. B., Schlax, M. G., & Samelson, R. M. (2011). Global observations of nonlinear mesoscale eddies. *Progress in Oceanography*, *91*(2), 167–216. https://doi.org/10.1016/j.pocean.2011.01.002

Comiso, J. C., Gersten, R. A., Stock, L. V., Turner, J., Perez, G. J., & Cho, K. (2016). Positive trend in the Antarctic sea ice cover and associated changes in surface temperature. *Journal of Climate*, *30*(6), 2251–2267. https://doi.org/10.1175/JCLI-D-16-0408.1

Cook, A. J., Fox, A. J., Vaughan, D. G., & Ferrigno, J. G. (2005). Retreating glacier fronts on the Antarctic Peninsula over the past half-century. *Science*, *308*(5721), 541–544. https://doi.org/10.1126/science.1104235

Cook, A. J., Holland, P. R., Meredith, M. P., Murray, T., Luckman, A., & Vaughan, D. G. (2016). Ocean forcing of glacier retreat in the western Antarctic Peninsula. *Science*, *353*(6296), 283–286. https://doi.org/10.1126/science.aae0017

Couto, N., Martinson, D. G., Kohut, J., & Schofield, O. (2017). Distribution of upper circumpolar deep water on the warming continental shelf of the West Antarctic Peninsula. *Journal of Geophysical Research: Oceans*, *122*, 5306–5315. https://doi.org/10.1002/2017JC012840

Dinniman, M. S., & Klinck, J. M. (2004). A model study of circulation and cross-shelf exchange on the west Antarctic Peninsula continental shelf. *Deep-Sea Research Part Ii-Topical Studies in Oceanography*, *51*, 2003–2022. https://doi.org/10.1016/j.dsr2.2004.07.030

Dinniman, M. S., Klinck, J. M., & Smith, W. O. (2011). A model study of Circumpolar Deep Water on the West Antarctic Peninsula and Ross Sea continental shelves. *Deep-Sea Research Part Ii-Topical Studies in Oceanography*, *58*, 1508–1523. https://doi.org/10.1016/j.dsr2.2010.11.013

Flagg, C. N., & Beardsley, R. C. (1978). Stability of shelf water-slope water front south of New England. *Journal of Geophysical Research*, *83*, 4623–4631. https://doi.org/10.1029/JC083iC09p04623

Fretwell, P., Pritchard, H. D., Vaughan, D. G., Bamber, J. L., Barrand, N. E., Bell, R., et al. (2013). Bedmap2: Improved ice bed, surface and thickness datasets for Antarctica. *The Cryosphere*, *7*(1), 375–393. https://doi.org/10.5194/tc-7-375-2013

Giorgetti, A., Crise, A., Laterza, R., Perini, L., Rebesco, M., & Camerlenghi, A. (2003). Water masses and bottom boundary layer dynamics above a sediment drift of the Antarctic Peninsula Pacific Margin. *Antarctic Science*, *15*, 537–546. https://doi.org/10.1017/S0954102003001652

Graham, J. A., Dinniman, M. S., & Klinck, J. M. (2016). Impact of model resolution for on-shelf heat transport along the West Antarctic Peninsula. *Journal of Geophysical Research: Oceans*, *121*, 7880–7897. https://doi.org/10.1002/2016JC011875

Griffiths, R. W., & Linden, P. F. (1981). The stability of buoyancy-driven coastal currents. *Dynamics of Atmospheres and Oceans*, *5*, 281–306. https://doi.org/10.1016/0377-0265(81)90004-X

Haidvogel, D. B., Arango, H., Budgell, W. P., Cornuelle, B. D., Curchitser, E., Di Lorenzo, E., et al. (2008). Ocean forecasting in terrain-following coordinates: Formulation and skill assessment of the Regional Ocean Modeling System. *Journal of Computational Physics*, *227*(7), 3595–3624. https://doi.org/10.1016/j.jcp.2007.06.016

Haine, T. W. N., & Marshall, J. (1998). Gravitational, symmetric, and baroclinic instability of the ocean mixed layer. *Journal of Physical Oceanography*, *28*(4), 634–658. https://doi.org/10.1175/1520-0485(1998)028<0634:GSABIO>2.0.CO;2

Häkkinen, S., & Mellor, G. L. (1992). Modeling the seasonal variability of a coupled Arctic ice-ocean system. *Journal of Geophysical Research*, *97*(C12), 20,285–20,304. https://doi.org/10.1029/92JC02037

Hillenbrand, C. D., Camerlenghi, A., Cowan, E. A., Hernández-Molina, F. J., Lucchi, R. G., Rebesco, M., & Uenzelmann-Neben, G. (2008). The present and past bottom-current flow regime around the sediment drifts on the continental rise west of the Antarctic Peninsula. *Marine Geology*, *255*(1), 55–63. https://doi.org/10.1016/j.margeo.2008.07.004

Hillenbrand, C.-D., & Ehrmann, W. (2005). Late Neogene to Quaternary environmental changes in the Antarctic Peninsula region: Evidence from drift sediments. *Global and Planetary Change*, *45*, 165–191. https://doi.org/10.1016/j.gloplacha.2004.09.006

Holland, D. M., & Jenkins, A. (1999). Modeling thermodynamic ice-ocean interactions at the base of an ice shelf. *Journal of Physical Oceanography*, *29*(8), 1787–1800. https://doi.org/10.1175/1520-0485(1999)029<1787:MTIOIA>2.0.CO;2

Holland, P. R., Jenkins, A., & Holland, D. M. (2010). Ice and ocean processes in the Bellingshausen Sea, Antarctica. *Journal of Geophysical Research*, *115*, C05020. https://doi.org/10.1029/2008JC005219

Hristova, H. G., Kessler, W. S., McWilliams, J. C., & Molemaker, M. J. (2014). Mesoscale variability and its seasonality in the Solomon and Coral Seas. *Journal of Geophysical Research: Oceans*, *119*, 4669–4687. https://doi.org/10.1002/2013JC009741

Hunke, E. C. (2001). Viscous–plastic sea ice dynamics with the EVP model: Linearization issues. *Journal of Computational Physics*, *170*(1), 18–38. https://doi.org/10.1006/jcph.2001.6710

Hunke, E. C., & Dukowicz, J. K. (1997). An elastic-viscous-plastic model for sea ice dynamics. *Journal of Physical Oceanography*, *27*(9), 1849–1867. https://doi.org/10.1175/1520-0485(1997)027<1849:AEVPMF>2.0.CO;2

Isachsen, P. E. (2011). Baroclinic instability and eddy tracer transport across sloping bottom topography: How well does a modified Eady model do in primitive equation simulations? *Ocean Modelling*, *39*, 183–199. https://doi.org/10.1016/j.ocemod.2010.09.007

Isern-Fontanet, J., García-Ladona, E., & Font, J. (2003). Identification of marine eddies from altimetric maps. *Journal of Atmospheric and Oceanic Technology*, *20*(5), 772–778. https://doi.org/10.1175/1520-0426(2003)20<772:IOMEFA>2.0.CO;2

Jacobs, S. S., Jenkins, A., Giulivi, C. F., & Dutrieux, P. (2011). Stronger ocean circulation and increased melting under Pine Island Glacier ice shelf. *Nature Geoscience*, *4*(8), 519–523. https://doi.org/10.1038/ngeo1188

King, J. C., Turner, J., Marshall, G. J., Connolley, W. M., & Lachlan-Cope, T. A. (2013). *Antarctic peninsula climate variability and its causes as revealed by analysis of instrumental records. In Antarctic Peninsula Climate Variability: Historical and Paleoenvironmental Perspectives* (pp. 17–30). Washington DC: American Geophysical Union (AGU). https://doi.org/10.1029/AR079p0017

Kurian, J., Colas, F., Capet, X., McWilliams, J. C., & Chelton, D. B. (2011). Eddy properties in the California Current System. *Journal of Geophysical Research*, *116*, C08027. https://doi.org/10.1029/2010JC006895

Martinson, D. G., & McKee, D. C. (2012). Transport of warm Upper Circumpolar Deep Water onto the western Antarctic Peninsula continental shelf. *Ocean Science*, *8*, 433–442. https://doi.org/10.5194/os-8-433-2012

Martinson, D. G., Stammerjohn, S. E., Iannuzzi, R. A., Smith, R. C., & Vernet, M. (2008). Western Antarctic Peninsula physical oceanography and spatio-temporal variability. *Deep-Sea Research Part Ii-Topical Studies in Oceanography*, *55*, 1964–1987. https://doi.org/10.1016/j.dsr2.2008.04.038

McKee, D. C., Martinson, D. G., & Schofield, O. (2019). Origin and attenuation of mesoscale structure in circumpolar deep water intrusions to an Antarctic shelf. *Journal of Physical Oceanography*, *49*(5), 1293–1318. https://doi.org/10.1175/JPO-D-18-0133.1

Mellor, G. L., & Kantha, L. (1989). An ice-ocean coupled model. *Journal of Geophysical Research*, *94*(C8), 10,937–10,954. https://doi.org/10.1029/JC094iC08p10937

Merckelbach, L., Smeed, D., & Griffiths, G. (2010). Vertical water velocities from underwater gliders. *Journal of Atmospheric and Oceanic Technology*, *27*, 547–563. https://doi.org/10.1175/2009JTECHO710.1

Meredith, M. P., & King, J. C. (2005). Rapid climate change in the ocean west of the Antarctic Peninsula during the second half of the 20th century. *Geophysical Research Letters*, *32*, L19604. https://doi.org/10.1029/2005GL024042

Moffat, C., Owens, B., & Beardsley, R. C. (2009). On the characteristics of Circumpolar Deep Water intrusions to the west Antarctic Peninsula Continental Shelf. *Journal of Geophysical Research*, *114*, C05017. https://doi.org/10.1029/2008JC004955

Orsi, A. H., Whitworth, T., & Nowlin, W. D. (1995). On the meridional extent and fronts of the Antarctic circumpolar current. *Deep-Sea Research Part I-Oceanographic Research Papers*, *42*, 641–673. https://doi.org/10.1016/0967-0637(95)00021-W

Pickart, R. S., Torres, D. J., & Fratantoni, P. S. (2005). The East Greenland Spill Jet. *Journal of Physical Oceanography*, *35*, 1037–1053. https://doi.org/10.1175/JPO2734.1

Plumb, R. A., & Ferrari, R. (2005). Transformed Eulerian-mean theory. Part I: Nonquasigeostrophic theory for eddies on a zonal-mean flow. *Journal of Physical Oceanography*, *35*(2), 165–174. https://doi.org/10.1175/JPO-2669.1

Powers, J. G., Manning, K. W., Bromwich, D. H., Cassano, J. J., & Cayette, A. M. (2012). A decade of Antarctic science support through amps. *Bulletin of the American Meteorological Society*, *93*(11), 1699–1712. https://doi.org/10.1175/BAMS-D-11-00186.1

Prezelin, B. B., Hofmann, E. E., Mengelt, C., & Klinck, J. M. (2000). The linkage between Upper Circumpolar Deep Water (UCDW) and phytoplankton assemblages on the west Antarctic Peninsula continental shelf. *Journal of Marine Research*, *58*, 165–202. https://doi.org/10.1357/002224000321511133

Rebesco, M., Larter, R. D., Camerlenghi, A., & Barker, P. F. (1996). Giant sediment drifts on the continental rise west of the Antarctic Peninsula. *Geo-Marine Letters*, *16*(2), 65–75. https://doi.org/10.1007/BF02202600

Reszka, M. K., & Swaters, G. E. (1999). Eddy formation and interaction in a baroclinic frontal geostrophic model. *Journal of Physical Oceanography*, *29*, 3025–3042. https://doi.org/10.1175/1520-0485(1999)029<3025:EFAIIA>2.0.CO;2

Rignot, E., Mouginot, J., Morlighem, M., Seroussi, H., & Scheuchl, B. (2014). Widespread, rapid grounding line retreat of Pine Island, Thwaites, Smith, and Kohler glaciers, West Antarctica, from 1992 to 2011. *Geophysical Research Letters*, *41*, 3502–3509. https://doi.org/10.1002/2014GL060140

Rignot, E., Mouginot, J., Scheuchl, B., van den Broeke, M., van Wessem, M. J., & Morlighem, M. (2019). Four decades of Antarctic Ice Sheet mass balance from 1979–2017. *Proceedings of the National Academy of Sciences*, *116*(4), 1095–1103. https://doi.org/10.1073/pnas.1812883116

Rio, M. H., Guinehut, S., & Larnicol, G. (2011). New CNES-CLS09 global mean dynamic topography computed from the combination of GRACE data, altimetry, and in situ measurements. *Journal of Geophysical Research*, *116*, C07018. https://doi.org/10.1029/2010JC006505

Savidge, D. K., & Amft, J. A. (2009). Circulation on the West Antarctic Peninsula derived from 6 years of shipboard ADCP transects. *Deep-Sea Research Part I-Oceanographic Research Papers*, *56*, 1633–1655. https://doi.org/10.1016/j.dsr.2009.05.011

Schloss, I., Abele, D., Moreau, S., Demers, S., Bers, V., González, O., & Ferreyra, G. (2012). Response of phytoplankton dynamics to 19-year (1991–2009) climate trends in Potter Cove (Antarctica) (Vol. 92). https://doi.org/10.1016/j.jmarsys.2011.10.006

Schmidtko, S., Heywood, K. J., Thompson, A. F., & Aoki, S. (2014). Multidecadal warming of Antarctic waters. *Science*, *346*(6214), 1227–1231. https://doi.org/10.1126/science.1256117

Shchepetkin, A. F., & McWilliams, J. C. (2009). Ocean forecasting in terrain-following coordinates: Formulation and skill assessment of the regional ocean modeling system. *Journal of Computational Physics*, *228*(24), 8985–9000. https://doi.org/10.1016/j.jcp.2009.09.002

Smith, K. S. (2007). The geography of linear baroclinic instability in Earth's oceans. *Journal of Marine Research*, *65*(5), 655–683. https://doi.org/10.1357/002224007783649484

Stammerjohn, S. E., Martinson, D. G., Smith, R. C., Yuan, X., & Rind, D. (2008). Trends in Antarctic annual sea ice retreat and advance and their relation to El Niño–Southern Oscillation and Southern annular mode variability. *Journal of Geophysical Research*, *113*, C03S90. https://doi.org/10.1029/2007JC004269

Steele, M., Mellor, G. L., & Mcphee, M. G. (1989). Role of the molecular sublayer in the melting or freezing of sea ice. *Journal of Physical Oceanography*, *19*(1), 139–147. https://doi.org/10.1175/1520-0485(1989)019<0139:ROTMSI>2.0.CO;2

Stewart, A. L., & Thompson, A. F. (2013). Connecting Antarctic cross-slope exchange with Southern Ocean overturning. *Journal of Physical Oceanography*, *43*(7), 1453–1471. https://doi.org/10.1175/JPO-D-12-0205.1

Stewart, A. L., & Thompson, A. F. (2015). Eddy-mediated transport of warm Circumpolar Deep Water across the Antarctic Shelf Break. *Geophysical Research Letters*, *42*, 432–440. https://doi.org/10.1002/2014GL062281

St-Laurent, P., Klinck, J. M., & Dinniman, M. S. (2013). On the role of coastal troughs in the circulation of warm circumpolar deep water on Antarctic Shelves. *Journal of Physical Oceanography*, *43*, 51–64. https://doi.org/10.1175/JPO-D-11-0237.1

Thompson, A. F., Heywood, K. J., Schmidtko, S., & Stewart, A. L. (2014). Eddy transport as a key component of the Antarctic overturning circulation. *Nature Geoscience*, *7*, 879–884. https://doi.org/10.1038/NGEO2289

Troupin, C., Beltran, J. P., Heslop, E., Torner, M., Garau, B., Allen, J., et al. (2016). A toolbox for glider data processing and management. *Methods in Oceanography*, *13-14*, 13–23. https://doi.org/10.1016/j.mio.2016.01.001

Turner, J., Colwell, S. R., Marshall, G. J., Lachlan-Cope, T. A., Carleton, A. M., Jones, P. D., et al. (2005). Antarctic climate change during the last 50 years. *International Journal of Climatology*, *25*(3), 279–294. https://doi.org/10.1002/joc.1130

Turner, J., Lu, H., White, I., King, J. C., Phillips, T., Hosking, J. S., et al. (2016). Absence of 21st century warming on Antarctic Peninsula consistent with natural variability. *Nature*, *535*(7612), 411–415. https://doi.org/10.1038/nature18645

Vaughan, D. G., Marshall, G. J., Connolley, W. M., Parkinson, C., Mulvaney, R., Hodgson, D. A., et al. (2003). Recent rapid regional climate warming on the Antarctic Peninsula. *Climatic Change*, *60*(3), 243–274. https://doi.org/10.1023/A:1026021217991

Venables, H. J., & Meredith, M. P. (2014). Feedbacks between ice cover, ocean stratification, and heat content in Ryder Bay, western Antarctic Peninsula. *Journal of Geophysical Research: Oceans*, *119*, 5323–5336. https://doi.org/10.1002/2013JC009669

Wadhams, P., Gill, A. E., & Linden, P. F. (1979). Transects by submarine of the East Greenland Polar Front. *Deep-Sea Research Part a-Oceanographic Research Papers*, *26*(12), 1311–1327. https://doi.org/10.1016/0198-0149(79)90001-3

Wallace, J. M., & Lau, N.-C. (1985). On the role of barotropic energy conversions in the general circulation. *Advances in Geophysics*, *28*, 33–74. https://doi.org/10.1016/S0065-2687(08)60219-8

Zhang, Y., Pedlosky, J., & Flierl, G. R. (2011). Cross-shelf and out-of-bay transport driven by an open-ocean current. *Journal of Physical Oceanography*, *41*, 2168–2186. https://doi.org/10.1175/JPO-D-11-08.1